nature plants

Article

https://doi.org/10.1038/s41477-024-01804-x

Molecular basis of plastoquinone reduction in plant cytochrome b_6f

Received: 19 April 2024

Accepted: 3 September 2024

Sebastian Pintscher[1,6,7], Rafał Pietras[2,7], Bohun Mielecki[2,3], Mateusz Szwalec[2], Anna Wójcik-Augustyn[2], Paulina Indyka[4], Michał Rawski[4], Łukasz Koziej[1], Marcin Jaciuk[1,4], Grzegorz Ważny[3,4], Sebastian Glatt[1,5] & Artur Osyczka[2]

A multi-subunit enzyme, cytochrome b_6f (cytb_6f), provides the crucial link between photosystems I and II in the photosynthetic membranes of higher plants, transferring electrons between plastoquinone (PQ) and plastocyanin. The atomic structure of cytb_6f is known, but its detailed catalytic mechanism remains elusive. Here we present cryogenic electron microscopy structures of spinach cytb_6f at 1.9 Å and 2.2 Å resolution, revealing an unexpected orientation of the substrate PQ in the haem ligand niche that forms the PQ reduction site (Q_n). PQ, unlike Q_n inhibitors, is not in direct contact with the haem. Instead, a water molecule is coordinated by one of the carbonyl groups of PQ and can act as the immediate proton donor for PQ. In addition, we identify water channels that connect Q_n with the aqueous exterior of the enzyme, suggesting that the binding of PQ in Q_n displaces water through these channels. The structures confirm large movements of the head domain of the iron–sulfur protein (ISP-HD) towards and away from the plastoquinol oxidation site (Q_p) and define the unique position of ISP-HD when a Q_p inhibitor (2,5-dibromo-3-methyl-6-isopropylbenzoquinone) is bound. This work identifies key conformational states of cytb_6f, highlights fundamental differences between substrates and inhibitors and proposes a quinone–water exchange mechanism.

Photosynthesis powers the metabolism of photoautotrophic organisms by converting solar energy into biologically useful forms of energy. In higher plants, photosynthesis is accomplished in the thylakoid membranes of chloroplasts by electron transport chains composed of two large membrane protein complexes—photosystems I and II—that are functionally linked by cytochrome b_6f (cytb_6f)[1–3]. By catalyzing the transfer of electrons from lipid-soluble plastoquinone (PQ) to water-soluble plastocyanin (PC), cytb_6f transfers electrons from photosystem II to photosystem I. This results in proton transfer across the membrane and contributes to the proton-motive force required for the production of adenosine triphosphate[4]. Cytb_6f is also involved in regulatory processes that secure photosynthetic efficiency[5–8]. Cytb_6f is, thus, a crucial enzyme for photosynthesis. Yet, some of the most fundamental aspects of its mechanism remain unclear.

Cytb_6f operates according to a modified 'Q-cycle' that was originally developed for cytochrome bc_1 (cytbc_1)[4,9]. Cytbc_1 is related to cytb_6f and performs a similar function in the respiratory or photosynthetic electron transport chains. By analogy to cytbc_1, the cycle in cytb_6f is

---

[1]Małopolska Centre of Biotechnology (MCB), Jagiellonian University, Kraków, Poland. [2]Faculty of Biochemistry, Biophysics and Biotechnology, Department of Molecular Biophysics, Jagiellonian University, Kraków, Poland. [3]Doctoral School of Exact and Natural Sciences, Jagiellonian University, Kraków, Poland. [4]National Synchrotron Radiation Centre SOLARIS, Jagiellonian University, Kraków, Poland. [5]Department for Biological Sciences and Pathobiology, University of Veterinary Medicine Vienna, Vienna, Austria. [6]Present address: Faculty of Biochemistry, Biophysics and Biotechnology, Department of Plant Biotechnology, Jagiellonian University, Kraków, Poland. [7]These authors contributed equally: Sebastian Pintscher, Rafał Pietras. e-mail: sebastian.glatt@uj.edu.pl; artur.osyczka@uj.edu.pl

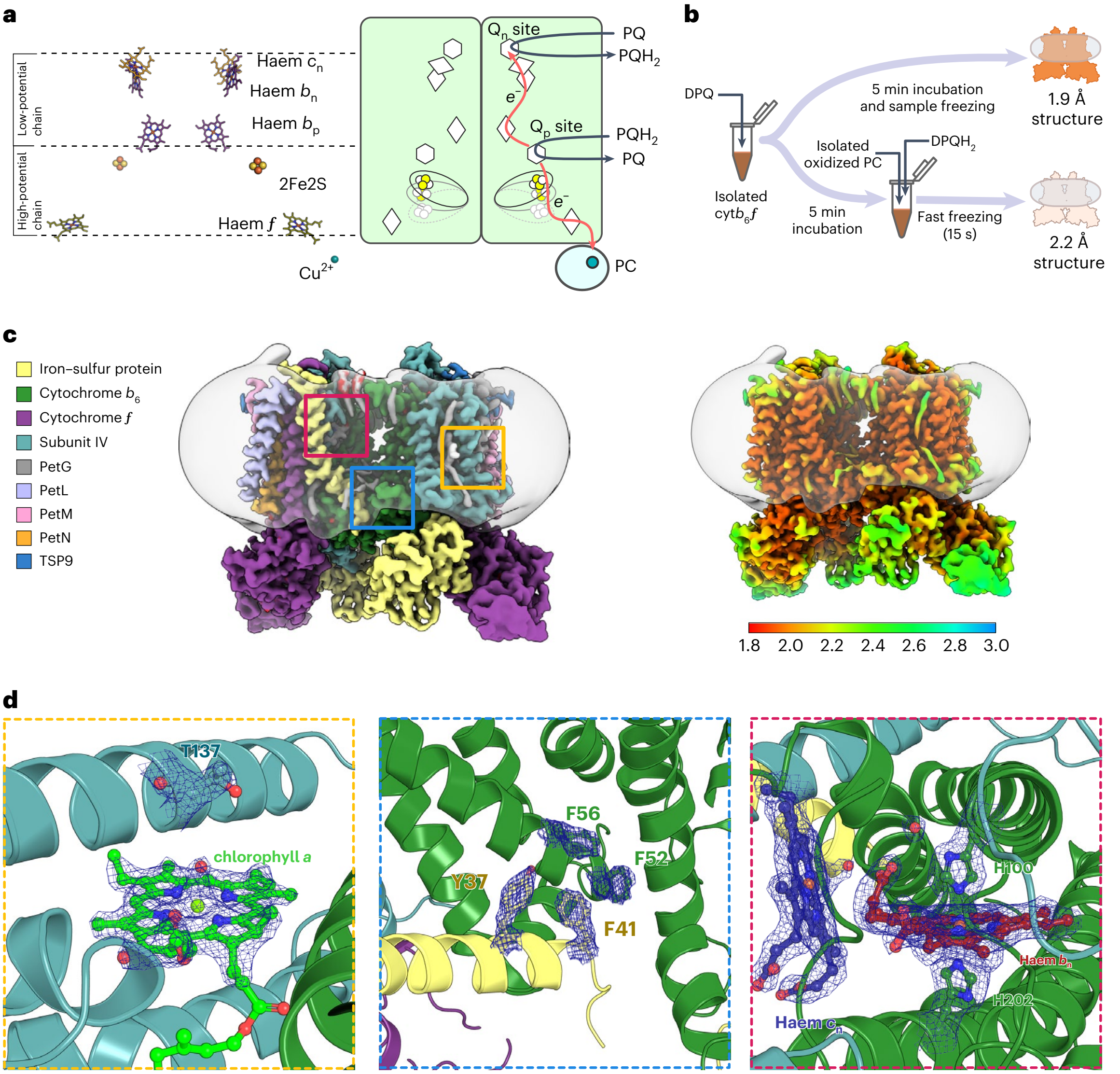

Fig. 1 | An overview of the structure of cytb_6f, cofactor architecture and sample preparation. a, Arrangement of redox cofactor chains in cytb_6f and a schematic representation of PQH_2 oxidation and PQ reduction at Q_p and Q_n, respectively. Green-filled boxes represent two monomers of cytb_6f. PC stands for plastocyanin. **b**, Two procedures for cryo-EM grid preparation, which yielded 1.9 Å and 2.2 Å cryo-EM maps for DPQ-incubated cytb_6f and cytb_6f during enzymatic turnover, respectively. **c**, Cryo-EM maps at 1.9 Å resolution of DPQ-incubated cytb_6f with colour-coded subunits (left) and coloured according to the calculated local resolution (in Å; right). **d**, Close-up view of selected 1.9 Å map regions with remarkable resolution of amino acid side chains and cofactors. The colours of the frames correspond to regions marked by squares in **c**.

based on the joint operation of two catalytic sites, Q_p and Q_n. These sites are located on opposite sides of the membrane and are responsible for plastoquinol (PQH_2) oxidation (at the Q_p site, on the luminal side of the membrane) and PQ reduction (at the Q_n site, on the stromal side)[10]. These sites are connected functionally by redox cofactors organized in two chains: a 'low-potential' chain comprising *b*-type haems b_p and b_n and *c*-type haem c_n (also referred to as haem c_i), and a 'high-potential' chain comprising an iron–sulfur cluster [2Fe2S] and a *c*-type haem *f*[11]. The Q_p acts as a branch point for both chains, where it is linked to Q_n in the low-potential chain and to PC in the high-potential chain (Fig. 1a). The oxidation of PQH_2 at Q_p separates the routes for two electrons deriving from this reaction. One electron is transferred to PC via the [2Fe2S] and haem *f*, and the other is transferred via haem b_p and the pair of haems b_n/c_n to ultimately reduce quinone at Q_n. As a consequence of the bifurcation reaction, the low-potential chain delivers one electron to Q_n at a time. Thus, the oxidation of two PQH_2 at Q_p leads to reduction of one PQ at Q_n, which results in a net oxidation of PQH_2 (refs. 3,6).

Various structures of cytbc_1 and cytb_6f show that the positions of cofactors are consistent with a functional Q-cycle in both complexes[12–22]. Nevertheless, intriguing differences between cytbc_1 and cytb_6f also indicate functional differences. For instance, the cytb_6f complex contains additional cofactors—chlorophyll *a*, 9-*cis* β-carotene and haem c_n—whose functions are unclear. Haem c_n is highly unusual. It is a high-spin haem with a water molecule as the only axial ligand to the haem iron. It is covalently attached to a single cysteine residue and positioned in proximity to haem b_n (refs. 15,16,20). Moreover, it occupies the position where ubiquinone binding occurs in cytbc_1. Haem c_n thus appears to be an extension of the low-potential chain (Fig. 1a), but the mechanistic consequences of this arrangement remain highly speculative. Inhibitors of Q_n have been shown to bind as axial ligands to haem c_n, and it has been postulated that the substrate binds in a similar way[17,18,23]. However, the reported positions of PQ in the region of Q_n are inconsistent with the overall model and, thus, have been considered precatalytic states[22,24].

Currently available structures of cytb_6f show a large distance between Q_p and haem f, similar to the large distance between Q_p and haem c_1 (equivalent of haem f) observed in cytbc_1. This implies that large-scale movement of the domain harbouring the iron–sulfur cluster (ISP-HD) between positions close to Q_p and haem f/c_1 must occur during the catalytic cycle[25]. Indeed, such movement is well documented for cytbc_1, not only by numerous spectroscopic and kinetic analyses[26–29] but also by structural data showing ISP-HD in various positions[30]. In the case of cytb_6f, spectroscopic data suggest a similar movement of ISP-HD[31–33]; however, distinct positions of ISP-HD have not yet been structurally characterized.

To simultaneously address these open questions, we determined high-resolution, single-particle cryogenic electron microscopy (cryo-EM) structures of spinach cytb_6f in various states (Fig. 1b). We show that decylplastoquinone (DPQ), an analogue of the natural PQ substrate, adopts an unprecedented position and orientation in the Q_n site during catalysis. The observed coordination is fundamentally different from the known position of Q_n site-specific inhibitors[17,18,23]. Our structures also reveal coordinated water channels that connect the exterior of the complex directly with Q_n. Furthermore, we show that ISP-HD adopts distinct positions, which illustrate its dynamic movement between cyt b_6 and cyt f. These findings provide fundamental molecular insights into the interactions at the catalytic sites of cytb_6f that inspire new concepts for explaining substrate exchange in cytb_6f and cytbc_1 complexes.

Table 1 | Cryo-EM data collection, refinement and validation statistics

	Cytb_6f+DPQ	Cytb_6f+DPQ+DPQH_2+PC	Cytb_6f+DBMIB
	PDB ID 9ES7	PDB ID 9ES8	PDB ID 9ES9
	EMD 19938	EMD 19939	EMD 19940
Data collection and processing			
Magnification of exposure image	×105,000	×105,000	×105,000
Operating voltage (kV)	300	300	300
Electron exposure (e^- Å^{-2})	40.70	40.70	41.34
Defocus range (μm)	−2.1 to −0.9	−2.1 to −0.9	−2.1 to −0.9
Pixel size (Å)	0.86	0.86	0.86
Symmetry imposed	*C*2	*C*2	*C*2
Final particle images	1,320,078	482,950	389,849
Map resolution (Å)	1.94	2.24	2.33
FSC threshold	0.143	0.143	0.143
Map resolution range (Å)	1.9 to >10	1.9 to >10	1.9 to >10
Refinement			
Initial model used (PDB ID)	7ZYV	7ZYV	7ZYV
Model resolution (Å)	2.1	2.1	2.1
FSC threshold	0.143	0.143	0.143
Model resolution range (Å)	NA	NA	NA
Map sharpening B factor (Å^2)	58.3	71.3	72.5
Model composition			
Non-hydrogen atoms	16,413	16,326	16,450
Protein residues	1,950	1,948	1,974
Ligands	22	24	24
Water molecules	329	214	206
B factors (Å^2)			
Protein	56.97	76.03	80.93
Ligands	55.97	80.25	85.03
Water molecules	57.21	71.37	78.49
RMS deviations			
Bond lengths (Å)	0.003	0.003	0.004
Bond angles (°)	0.514	0.482	0.983
Validation			
MolProbity score	0.94	0.99	1.31
Clashscore	1.81	1.72	3.25
Poor rotamers (%)	0.37	0.37	0.61
Ramachandran			
Favoured (%)	98.43	97.69	96.79
Allowed (%)	1.57	2.31	3.21
Disallowed (%)	0	0	0
CC volume	0.90	0.88	0.87

FSC, Fourier Shell Correlation; NA, not applicable; RMS, root mean squared; Clashscore, number of steric clashes per 1000 atoms in a model; CC, correlation coefficient.

Results

Cryo-EM structures of cytb_6f with DPQ and during turnover

Purified and detergent-solubilized cytb_6f was equilibrated with an excess of DPQ or exposed to substrates, reduced DPQ (DPQH_2) and oxidized PC and vitrified during catalytic turnover. These samples were used for single-particle cryo-EM analyses and resulted in two high-resolution reconstructions. In detail, we determined the structure of cytb_6f supplemented with DPQ at an overall resolution of 1.9 Å and the enzyme during catalysis at an overall resolution of 2.2 Å (Fig. 1b, Table 1 and Extended Data Fig. 1). Both structures show cytb_6f as a homodimeric complex with a subunit composition and spatial arrangement of cofactors consistent with previous reports[15,21,22] (Fig. 1c and Extended Data Fig. 1). The recently identified subunit thylakoid soluble phosphoprotein 9 (TSP9)[21] is present in both structures, indicating that it is stably associated throughout the catalytic cycle. The quality of the cryo-EM maps obtained allowed us to unambiguously identify amino acid side chains, ligands and cofactors (Fig. 1d). Furthermore, we observed density peaks in various regions of cytb_6f that likely correspond to coordinated water molecules, which we would expect to observe at 1.9 Å and 2.2 Å resolution. We assigned, validated and manually curated the positions of 329 water molecules in the 1.9 Å structure and 214 in the 2.2 Å structure.

DPQ does not contact the haem iron when bound at Q_n

The 2.2 Å resolution structure of cytb_6f vitrified during catalysis revealed the position and orientation of a quinone bound in Q_n (Fig. 2a,b). Note that we use the term 'quinone' to indicate a quinone group, not its redox state, which cannot be inferred from the cryo-EM maps. In detail, the quinone head is inclined at an angle of 37° relative to the plane of haem c_n, with the C4-side of the quinone ring positioned close to the haem plane (Fig. 2b,c). A water molecule (wat1) is coordinated between the carbonyl oxygen at the C4-side (O4) of quinone and the conserved Asp35 residue of subunit IV (D35$^{\mathrm{sIV}}$; Fig. 2b). D35$^{\mathrm{sIV}}$ and wat1 are located inside a hydrophobic pocket formed by F40$^{\mathrm{sIV}}$, L36$^{\mathrm{sIV}}$, A31$^{\mathrm{sIV}}$ and Val26 of the cytochrome b_6 subunit (V26$^{\mathrm{b6}}$) near haem c_n (Extended Data Fig. 2a). On the opposite side of the quinone group, the propionate of haem c_n and R207$^{\mathrm{b6}}$ enclose the carbonyl oxygen (O1) of DPQ (Fig. 2b and Extended Data Fig. 2b). O1 is close enough to R207$^{\mathrm{b6}}$ and the proximal propionate to hydrogen bond with them. The distal propionate points towards a hydrophilic tunnel comprising K24$^{\mathrm{b6}}$, N25$^{\mathrm{sIV}}$ and the backbone carbonyls of R207$^{\mathrm{b6}}$, K208$^{\mathrm{b6}}$ and Q209$^{\mathrm{b6}}$ (Extended Data Fig. 2b). The position of wat1 is remarkable because it suggests that this water molecule might be directly engaged in PQ reduction.

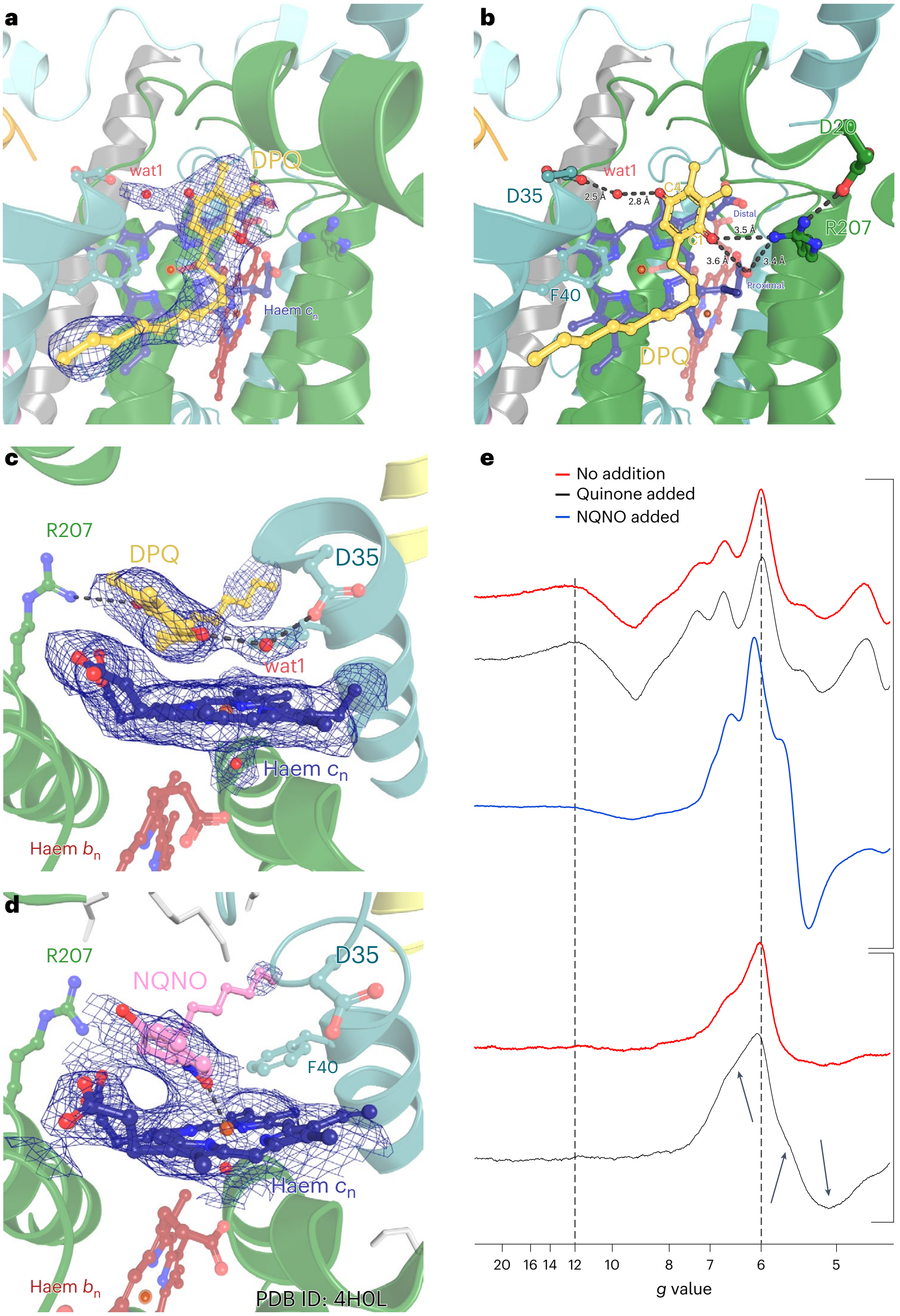

Fig. 2 | Q_n of cytb_6f occupied with DPQ molecule or inhibitor, NQNO. **a**, Quinone molecule (DPQ in all figures refers to a DPQ molecule, not its redox state) remodelled in the Q_n site in the 2.2 Å cryo-EM map (PDB ID: 9ES8). **b**, Hydrogen-bond interactions between quinone, wat1, haem c_n and selected residues. Cyt b_6 (green), subIV (light teal) and haem b_n (red) are in the background. **c**, Close-up side view of Q_n with quinone and haem c_n built into the cryo-EM map shown with isomesh representation. **d**, Close-up view of Q_n occupied by the NQNO inhibitor bound to haem c_n. The model and electron density map (that is, x-ray crystallographic $2F_o$–F_c map) were taken from PDB ID: 4H0L entry[17]. **e**, Low-field regions of the EPR spectra of cytb_6f poised at E_h of +180 mV or −20 mV, with (black) and without (red) addition of quinone. Black arrows indicate the regions with the largest observed changes, related to an increase in the rhombicity of the haem c_n signal in the sample with quinone added. For comparison, the blue spectrum shows the relatively larger effect on the rhombicity of the haem c_n signal imposed by interaction with NQNO bound at Q_n.

The orientation of the quinone ring in Q_n clearly differs from those of three Q_n inhibitors described previously: 2-nonyl-4-hydroxyquinoline *N*-oxide (NQNO), tridecyl-stigmatellin and stigmatellin A. In currently known structures of cytb_6f, these inhibitors coordinate the iron atom of haem c_n directly[17,18,23] (Fig. 2d and Extended Data Fig. 3). By analogy to these inhibitors, PQ was thought to bind to the haem c_n in the same way. Our structure, however, clearly shows that although the quinone ring is in proximity to the haem, there are no direct contacts between the quinone and the haem iron (Fig. 2c). In fact, the phenyl group of F40$^{\mathrm{sIV}}$ covers a large part of the haem plane, severely restricting access for the potential axial ligand[15,34]. We conclude that the inhibitors must push the F40$^{\mathrm{sIV}}$ ring away upon binding to occupy the Q_n niche and replace wat1.

The proximity of the quinone ring to haem c_n was further substantiated by the sensitivity of the electron paramagnetic resonance (EPR) spectrum of this haem to the redox state of quinone (Fig. 2e), observed as changes in transitions at different g values (the g factor, abbreviated as g, characterizes magnetic moment and angular momentum of molecular system with unpaired electrons). At a high external redox potential (E_h = +180 mV), the spectrum showed a $g = 12$ transition that originates from the spin–spin exchange between the oxidized haems c_n and b_n (ref. 35) and the $g = 6$ signal, which can be ascribed to a fraction of nearly axial high-spin haem c_n that is not spin-coupled to haem b_n (ref. 36). This spectrum was insensitive to the presence of externally added DPQ (at this E_h, quinone remains oxidized). At a lower E_h (−20 mV), the signal at $g = 12$ disappeared[37], but the remaining transitions around $g = 6$ were clearly sensitive to the presence of $DPQH_2$ in the sample (at this E_h, the added DPQ becomes fully reduced). Changes in the shape of the lines around $g = 6$ suggest a slight increase in the rhombicity of the zero-field splitting[36]. Typically, an increase in rhombicity is recognized by splitting of the $g = 6$ line into two lines. In our case, the rhombicity is not large, and the split is small and results in overlapping transitions (arrows in Fig. 2e). Such spectral change is possibly a consequence of lowering the symmetry of the ligand field around the iron ion of haem c_n, resulting from the presence of the quinone molecule nearby. However, we cannot conclude on the specific redox state of that molecule (that is, whether it is $DPQH_2$ or the semiquinone form) involved in these interactions.

NQNO, which binds as a ligand to the iron of haem c_n, induced different changes in the shape of the EPR spectrum (Fig. 2e, blue). Consistent with earlier observations[36], even at high E_h, a dramatic increase in the rhombicity of the signal was accompanied by loss of the signal at $g = 12$. Thus, the EPR spectra not only confirm the proximity of the quinone or inhibitor to haem c_n but also corroborate their different binding modes.

Proton channels and water molecules link Q_n to the exterior

The 4 Å distance between haem c_n and the quinone ring in the haem ligand niche confirms their readiness for the catalytically relevant electron transfer. Furthermore, hydrogen bonding indicates that the quinone is also ready to accept protons at O1 and O4, which are required for the completion of catalytic reduction of PQ (Figs. 2b and 3a). Wat1 is positioned to act as the primary proton donor for O4. Wat1 might accept a proton directly from $D35^{sIV}$, which is surrounded by several polar residues ($R26^{PetN}$, $E29^{sIV}$, $K272^{f}$ (transmembrane helix of the cytochrome f subunit)), and several aligned water molecules extending towards the aqueous phase (Fig. 3a–d, red dots). On the other side of the ring, $R207^{b6}$ is the most likely primary proton donor for O1; however, direct protonation by the proximal propionate of haem also appears possible. $R207^{b6}$ might accept protons from $D20^{b6}$, which is in direct contact with the protein exterior. Thus, these two residues might form an anhydrous proton channel towards O1, as proposed earlier[17]. $R207^{b6}$ might also accept a proton from the proximal propionate of haem (Fig. 2b).

In addition to the proton channels, our structures reveal channels filled with water molecules that line up, linking the Q_n niche with the aqueous phase outside the membrane (Fig. 3). In one channel, water molecules (Fig. 3, blue dots) are located in the crevice between subunit IV and cytb_6. They interact with the backbone atoms of $A31^{sIV}$, $W32^{sIV}$, $T22^{b6}$, $K24^{b6}$ and $I21^{b6}$ (Fig. 3b,c,e). Two water molecules are positioned within hydrogen-bonding distance to the side chain of $R207^{b6}$ (Fig. 3c). In another channel, the water molecules (Fig. 3, magenta dots) interact with the backbone atoms of $G23^{sIV}$, $Q209^{b6}$, $R207^{b6}$ and the side chains of $N25^{sIV}$ and $K24^{b6}$, reaching the distal propionate of haem c_n (Fig. 3b,c,f). We note that the density map of the region of the Q_n cavity in the 1.9 Å structure was not completely empty and may have been partially occupied by DPQ or endogenous quinone molecules. Nevertheless, two water molecules that are hydrogen-bonded by $R207^{b6}$ can be clearly identified. When quinone occupies the catalytically relevant position (as seen in the 2.2 Å structure), these water molecules would clash with the quinone ring and, thus, must be displaced during the full accommodation of quinone in the site.

We propose a mechanism in which the water channels allow water molecules to flow into and out of the Q_n cavity during catalysis (Fig. 3g). Quantum mechanical calculations indicate that in the absence of substrate (Fig. 3g, state 1), the Q_n cavity can be occupied by at least eight water molecules (including wat1), which shield the charged residues—$D20^{b6}$, $K24^{b6}$, $R207^{b6}$, $D35^{sIV}$ and $R26^{PetN}$ (Extended Data Fig. 4)—thereby weakening the interactions between them. This substantially reduces the binding energy of PQ, which, upon entering Q_n, pushes the water molecules out of the cavity through the channels in a piston-like manner (Fig. 3g, state 2). The only remaining water molecule is wat1, which allows the quinone ring to adopt an orientation that allows electron and proton transfer to O1 and O4 (Fig. 3g, state 3). When reduction of PQ is complete, PQH_2 leaves Q_n and exposes charged residues, attracting water molecules into Q_n through the channels (Fig. 3g, state 4). The Q_n site, filled with water (state 1), is then free to accommodate the next PQ molecule. In this mechanism, synchronized movements of water and PQ/PQH_2 facilitate exchange of the substrate/product and thus enable high efficiency of catalytic turnover.

It has been observed that the redox midpoint potential of haem c_n shows a strong dependence of −60 mV per pH unit[38], which implicates a coupled protonation event. This is not typical for haems in a protein environment. The enhanced exposure of haem c_n to water molecules, which can fill the quinone-binding cavity through the water channels, might contribute to the increased pH sensitivity of the redox potential of this haem. In addition, the biphasic titrations of this haem in the presence of NQNO implicate that the occupancy of the Q_n site is sensitive to the redox state of the enzyme[38]. The differences in the density maps of this region in our two samples (1.9 Å and 2.2 Å structure) are in line with these observations. Given that the redox state of haem c_n has also been shown to be sensitive to the membrane potential[39], the influence of membrane potential on occupancy of the Q_n site is to be considered. Haem c_n could play a role of the redox sensor to accommodate the catalytic reactions at the Q_n site to the dynamically changing redox state of the cells, but such scenarios require further experimental testing.

The proton transfer paths towards O1 and O4 of DPQ described here confirm earlier predictions from analyses of the cytb_6f structures with inhibitors bound at Q_n (ref. 17). Moreover, our work adds structural details essential for mechanistic considerations. First, wat1 is the primary proton donor for PQ, and it bridges between $D35^{sIV}$ and O1 to facilitate proton transfer. Second, the identified water channels and water-mediated networks of hydrogen bonds implicate a water–PQ exchange mechanism at Q_n.

The position of DPQ in our structure differs from the positions described earlier for PQ in cytb_6f of plants[22] and cyanobacteria[24]. In those structures, the angles between the PQ ring and the haem c_n plane differed from the angles in our structure. Moreover, the PQ ring pointed away from the haem ligand niche, closer to the side of the haem plane and closer to the inter-monomer cavity (Extended Data Fig. 5). Furthermore, in those orientations, PQ was unable to interact with protonable groups in a way that would allow both O1 and O4 to form hydrogen bonds at the same time. As our structure indicates, to achieve such an orientation, the PQ ring must enter the haem c_n ligand niche as deeply as the space allows. Incidentally, the PQ ring, in such a position, is relatively close to the protein surface and the cytb_6f-bound part of the TSP9 protein for potential interactions with redox partners that are postulated to deliver electrons to Q_n from the protein exterior as part of the cyclic electron flow in photosynthesis. The positions of PQ in Q_n reported previously might still be relevant to the states during the arrival or departure of PQ to or from the catalytic site.

Interestingly, the TSP9 fragment bound to cytb_6f appears to cover the salt bridge formed between the carboxylate group of the C-terminus of cyt b_6 and $R125^{sIV}$. This hinders the accessibility of $R125^{sIV}$

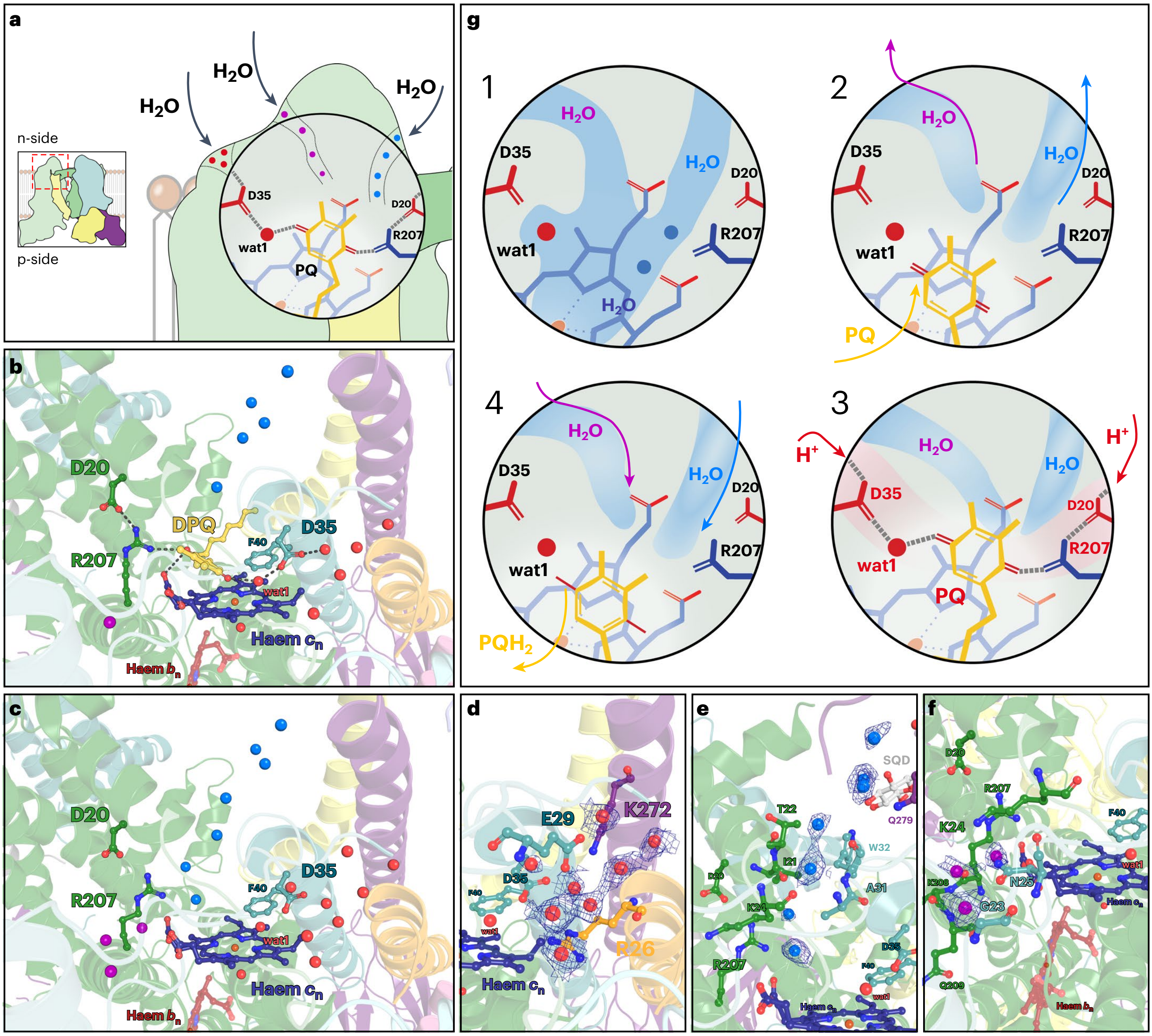

Fig. 3 | Water channels towards the cavity of Qn. a, Schematic representation of water chains connecting the Q_n cavity with the aqueous phase. The stromal and lumenal side of the thylakoid membrane are referred to as n-side and p-side, respectively. Red dots mark water molecules present in a funnel-like pocket in the cytb_6f surface, in contact with wat1 through D35$^{\mathrm{sIV}}$. Purple dots represent water molecules reaching the distal propionate of haem c_n. Blue dots represent a water molecule wire connected to R207^{b6}. **b**, The 2.2 Å structure of Q_n (PDB ID: 9ES8) with quinone bound, showing water molecules colour-coded the same as in **a**. **c**, The 1.9 Å structure of Q_n (PDB ID: 9ES7) showing water molecules colour-coded the same as in **a**. **d**–**f**, Close-up view of each water chain (red (**d**), blue (**e**) and purple (**f**)) taken from the 1.9 Å structure with selected amino acids and isomesh representation of the cryo-EM map around water molecules. **g**, The proposed quinone/water exchange mechanism as a molecular basis for the efficiency of catalytic turnover. In this mechanism, the arrival or departure of PQ from Q_n is synchronized with the movement of water molecules in and out of Q_n (see details in the text). Wat1 and the two water molecules seen in the 1.9 Å structure that clash with quinone in the 2.2 Å structures are marked as red and blue dots, respectively.

for interaction with a specific kinase involved in state transitions, as part of the regulatory function of cytb_6f (refs. 7,40). Furthermore, the carboxyl group of E50$^{\mathrm{TSP9}}$ forms another salt bridge with R125$^{\mathrm{sIV}}$, which additionally stabilizes this conformation (Extended Data Fig. 6). How R125$^{\mathrm{sIV}}$ becomes exposed to interact with the kinase remains to be elucidated.

ISP-HD adopts several positions between Q_p and haem *f*

On the other side of the membrane from Q_n, the other catalytic site in cytb_6f, Q_p, oxidizes PQH_2 to PQ. For this region, focused three-dimensional (3D) classifications of our cryo-EM datasets identified four distinct classes, representing the most populated states of cytb_6f present in the samples (Fig. 4a). These classes correspond to states in which ISP-HD occupies either the *b*-position (ISP-HD close to cyt b_6 and the Q_p site), the *f*-position (ISP-HD close to cyt *f*, with [2Fe2S] located close to haem *f*) or an intermediate position. An additional class corresponding to ISP-HD in an intermediate position with PC bound near cyt *f* was observed. Binding occurs in the same region as previously described[21]. The presence of these different states in the same dataset confirms the dynamic behaviour of ISP-HD and provides

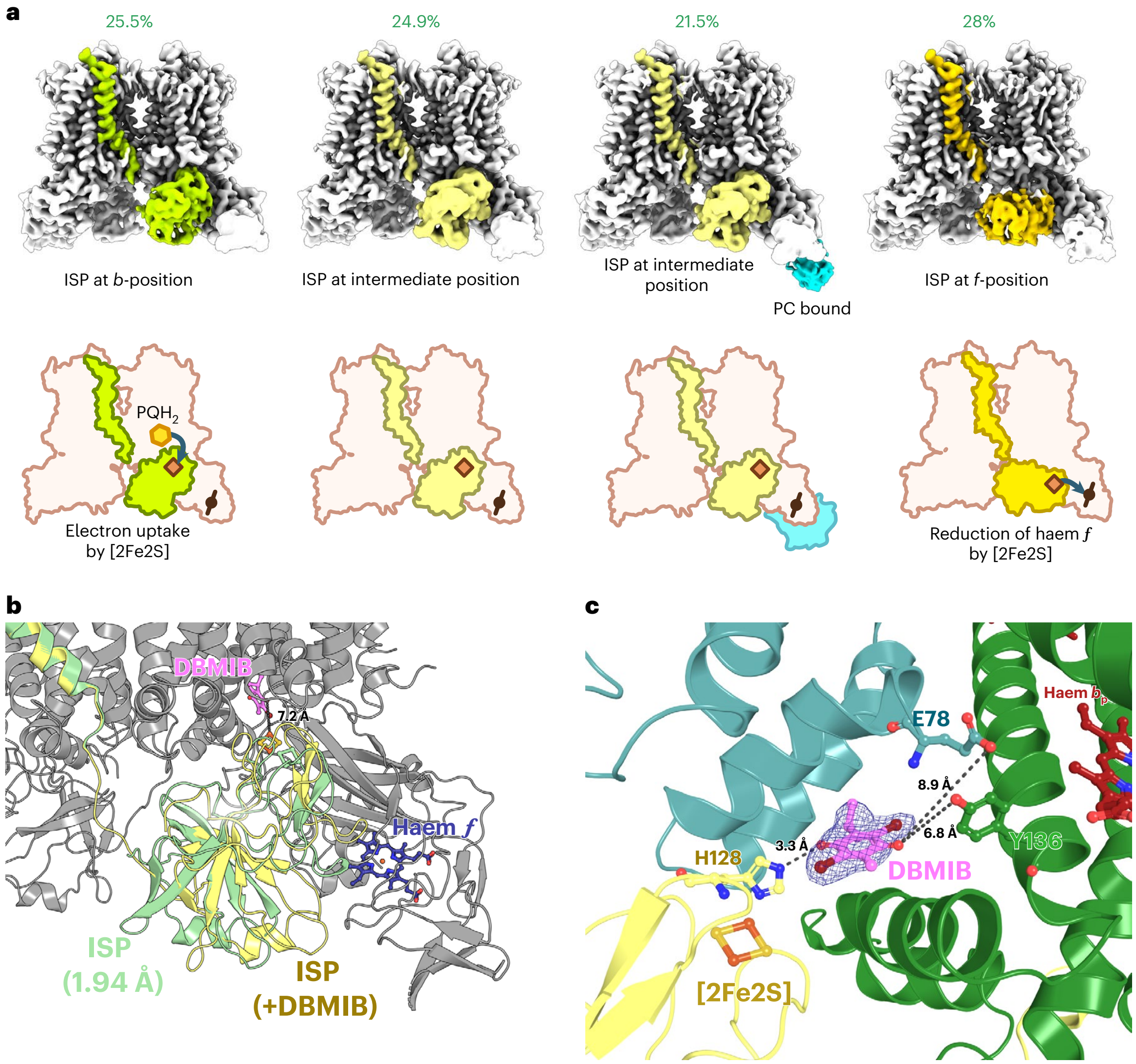

Fig. 4 | Heterogeneity of ISP-HD positions and binding of inhibitor DBMIB at Q_p. a, Three-dimensional classification of cytb_6f particles trapped during catalysis with different ISP-HD and PC positions with percentage results. Top: cryo-EM maps with colour-marked ISP subunit and PC. Bottom: schematic representation of ISP-HD and PC positions in each subgroup of particles. **b**, ISP-HD position in the cytb_6f structure with bound DBMIB (yellow; 2.3 Å; PDB ID: 9ES9) compared with the ISP-HD position from the 1.9 Å structure (green; PDB ID: 9ES7). **c**, Close-up view of Q_p occupied by DBMIB. DBMIB is within hydrogen-bond distance of the $N^ε$ atom of the H128 side chain, which also coordinates the 2Fe2S cluster via $N^δ$.

direct structural evidence for its movement, which is postulated to be necessary for catalysis. The *b*-position seems to reflect the state where electron transfer between 2Fe2S and PQ at the Q_p site takes place, and the *f*-position the state where electron transfer between the [2Fe2S] and haem *f* takes place (Fig. 4 and Extended Data Fig. 7).

In spectroscopic studies, the cytb_6f inhibitor 2,5-dibromo-3-methyl-6-isopropylbenzoquinone (DBMIB) was found to affect the position of ISP-HD[32,41,42]; therefore, we used it as a probe to further investigate ISP-HD movement. We determined the structure of DBMIB-inhibited cytb_6f at 2.2 Å resolution. In the presence of the inhibitor, only one state of ISP-HD was seen in the dataset. Remarkably, in this structure, ISP-HD was even closer to Q_p (Fig. 4b,c). The DBMIB molecule was clearly visible in our reconstruction. A hydrogen bond formed between the carbonyl group of the inhibitor and the $N^ε$ atom of $H128^{ISP}$, which coordinates the 2Fe2S cluster. $Y136^{b6}$ adopts two conformations (Extended Data Fig. 8a,b), one of which stabilizes DBMIB by forming a second hydrogen bond. In contrast to a previous report[43], these data clearly reveal the position of DBMIB in the active site of cytb_6f. Consistent with the inhibitory effect of this compound, its influence on the EPR spectrum of the [2Fe2S] cluster and observations based on EPR analysis, DBMIB traps ISP-HD at Q_p in the *b*-position[32,41,44]. Whether the extremely close position of ISP-HD in complex with DBMIB is a catalytically relevant position remains to be elucidated.

In the DBMIB-bound structure, unlike in other available structures, the first seven amino acids at the N-terminus, preceding the α-helical transmembrane anchor of ISP-HD, become structured (Extended Data Fig. 8c,d). The N-terminus bends towards the protein surface and interacts hydrophobically with cyt *f*. This change in position of this region might be relevant to cytb_6f -mediated redox sensing and signal transduction[42,45,46].

In all observed states, the 'neck' region that connects ISP-HD to its membrane anchor remains highly unstructured (Extended Data Fig. 9a–c). Only in the cryo-EM map with DBMIB, where the ISP-HD occupies the closest *b*-position, is the neck region slightly better resolved (Extended Data Fig. 9c). Therefore, the dynamic conformation of the neck region in cytb_6f is clearly different from that of cytbc_1, which undergoes a sharp transition from a stretched coil-like thread to a proper α-helix when ISP-HD occupies the *b*-position or the c_1-position[47]

(Extended Data Fig. 9d,e). The lack of an α-helix in the state where ISP-HD is in the *f*-position (corresponding to the c_1-position of cyt*bc*$_1$) implies that the motion of ISP-HD in cyt*bc*$_1$ and cytb_6f involves different transitions between conformations.

The position and orientation of the substrate (PQH_2) in Q_p for the catalytic reaction remain unresolved. In the internal cavities around Q_p, both 1.9 Å and 2.2 Å structures show densities remarkably similar to those described in the previous high-resolution structure of cytb_6f, which were interpreted as a possible channel for unidirectional PQ traffic through the site[21] (Extended Data Fig. 10). Nevertheless, some shortened density fragments might suggest that a partial replacement of natural PQ with the shorter PQ analogue DPQ has taken place. Ligands in the channel remain highly mobile, which makes unambiguous interpretation of their orientation as challenging as in previous analyses.

Conclusion

We present structural and spectroscopic data that point towards fundamentally different binding modes for substrates and inhibitors at the quinone reduction site of cytb_6f. Furthermore, we propose a quinone–water exchange mechanism that provides the molecular basis for effective catalytic turnover. Our data reveal overall similarities and minor differences in the motion of ISP-HD in cytb_6f compared with cyt*bc*$_1$. The structures also clarify the mechanism of cytb_6f inhibition by DBMIB at the Q_p site. Our findings contribute to a complete molecular description of the dynamic mechanisms of quinone oxidation and reduction reactions in cytb_6f. This work helps us understand the phenomena responsible for photosynthesis and respiration, which enable life on our planet.

Methods

Materials

Buffers, salts and DPQ were purchased from Sigma-Aldrich. Undecyl α-D-maltoside (UDM) was from Glycon. The propyl-sepharose resin was prepared by activating Sepharose-CNBr powder (Cytiva) and reacting it with propylamine (Sigma-Aldrich) according to the supplier's manual. NQNO (CAS 316-66-5) was purchased from Santa Cruz Biotechnology, and DBMIB (CAS 29096-93-3) was purchased from Sigma-Aldrich.

Purification of PC and cytb_6f

PC was purified according to the protocol described in ref. 21. To isolate and purify cytb_6f from spinach leaves, we used an optimized version of our previously published protocol (protocol 2 from ref. 21). The leaves were processed in a slow juicer with the addition of a cold buffer solution containing 50 mM Tris–HCl pH 8, 200 mM NaCl and 5 mM $MgCl_2$ (buffer 1). The resulting suspension was filtered through a sieve and a bag filter before being subjected to centrifugation at 8,000*g* for 20 min at 4 °C. The pellet containing chloroplasts was then resuspended in buffer 1 and diluted to a chlorophyll concentration of approximately 2.0 mg ml^{-1}. The chlorophyll content was estimated using the protocol described in ref. 48. The chloroplast suspension was cooled to 4 °C and sonicated with a 500 W ultrasonic processor (VCX 500) equipped with a 13 mm tip. The ultrasonic pulse sequence parameters were set as follows: 50% power, a pulse length of 30 s, a pulse interval of 60 s and a total pulse time of 8 min. Following sonication, the suspension was ultracentrifuged at 148,000*g* for 20 min at 4 °C. The pellet, consisting of thylakoid membranes, was resuspended in buffer 2 (50 mM Tris–HCl, pH 8.0, 50 mM NaCl), homogenized using a glass homogenizer and diluted to a chlorophyll concentration of 3.0 mg ml^{-1}. Solubilization of the thylakoid membranes was achieved by mixing an equal volume of thylakoid suspension and buffer 2 with the addition of 12 mg ml^{-1} UDM (final UDM-to-chlorophyll ratio was 4:1). The solution was stirred for 15 min and ultracentrifuged twice at 148,000*g* for 20 min at 4 °C. To avoid excessively high UDM concentrations in subsequent steps, the supernatant was precipitated with PEG using the following procedure. A solution consisting of 60% (w/w) PEG 4000 in buffer 2 was gradually added to the solubilized thylakoid solution until it became cloudy, resulting in a final PEG concentration of approximately 30%. The resulting suspension was then centrifuged for 10 min at 6,000*g* at 4 °C, and the supernatant was carefully separated from the pellet. The pellet was collected and solubilized in buffer 2 supplemented with 1 mM UDM (buffer 3). Then, solid ammonium sulfate was added to the solution to achieve 37% ammonium sulfate saturation. The solution was stirred for 15 min, centrifuged at 24,000*g* for 25 min at 4 °C and filtered through a 0.22 µm syringe filter before loading onto a propyl-sepharose column pre-equilibrated with buffer 3 at 37% ammonium sulfate saturation (buffer 4). The column was washed with 5 column volumes of buffer 4, and the greenish-brown band containing cytb_6f was eluted with buffer 3 at 20% ammonium sulfate saturation. The eluent was then brought back to 37% ammonium sulfate, centrifuged at 24,000*g* for 20 min at 4 °C and filtered through a 0.22 µm syringe filter. The sample was subsequently loaded onto a second propyl-sepharose column pre-equilibrated with buffer 4. The column was washed with 1 column volume of buffer 4 and 5 column volumes of buffer 3 at 30% ammonium sulfate saturation. The brownish band containing cytb_6f was eluted with buffer 3 at 25% ammonium sulfate saturation. The collected cytb_6f was then pooled, desalted and concentrated using an Amicon Ultra 50 kDa filter. The concentration of cytb_6f was assessed by measuring ascorbate-reduced minus ferricyanide-oxidized optical spectra at 554 nm, relative to the isosbestic point at 543 nm, using the differential extinction coefficient of haem *f* of cyt *f* $\varepsilon_{554-543} \approx 25$ mM^{-1} cm^{-1}. The sample was loaded onto a 10–22% continuous sucrose gradient made by a freeze–thaw method in buffer 3 and ultracentrifuged at 141,000*g* for 16 h at 4 °C.

Enzymatic activity measurement

The enzymatic activity of cytb_6f was measured spectrophotometrically (SHIMADZU UV-2450) by monitoring the reduction of PC at 597 nm using a procedure similar to that described in ref. 21. Briefly, the experiment was carried out in 50 mM HEPES (pH 7), 50 mM NaCl and 1 mM UDM, with 5 µM oxidized PC present. After initializing the measurement, $DPQH_2$:DPQ (1:1 mixture) was added to the reaction mixture to a final concentration of 10 µM each. Then, cytb_6f was added (final concentration of 2 nM) to the mixture to start the enzymatic reaction. The activity of cytb_6f was determined from the initial slope of the PC reduction curve, using a PC extinction coefficient $\varepsilon_{597} = 4.5$ mM^{-1} cm^{-1}. The activity rate for pure cytb_6f was estimated to be 110 s^{-1}. Cytb_6f inhibited by DBMIB (cytb_6f with a 10-fold excess of DBMIB incubated for 30 min before measurement) was not active.

Preparation of cryo-EM samples

Before the preparation of the cryo-EM samples, purified proteins were transferred to HEPES buffer (50 mM HEPES, 50 mM NaCl, 1 mM UDM, pH 7). For the preparation of DPQ supplemented and catalytic samples, purified cytb_6f was concentrated to about 170 µM (calculated as the concentration of cyt *f*). Then, 53 µl cytb_6f stock solution was mixed with 95 µl buffer and 1.5 µl stock DPQ solution (60 mM in DMSO). After about 5 min incubation with DPQ, 3 µl of the sample was applied to the grid and vitrified. For the catalytic sample, 29 µl of oxidized PC (2.1 mM) solution was added to the previously prepared mixture. After a short incubation with PC (about 1 min), 3 µl stock $DPQH_2$ solution (24 mM in EtOH/DMSO) was added. Immediately after $DPQH_2$ addition, 3 µl of the sample was applied to the grid and vitrified. The total time between the addition of $DPQH_2$ and sample vitrification was 15 s, measured using a digital stopwatch. It was verified spectroscopically that at the time of vitrification the PC was not fully reduced in the reaction mixture. Full reduction of PC in that mixture was observed several seconds after vitrification. The sample with DBMIB was prepared separately by mixing 12 µl of cytb_6f (153 µM, based on cyt *f* concentration) with 17 µl of buffer and 1 µl of 50 mM DBMIB. After 5 min incubation, 3 µl of the mixture was applied to the grid and vitrified. In all cases, the blotting and vitrification procedures were the same. Shortly before use, transmission electron microscopy grids (Quantifoil R2/1, Cu 200 mesh) were glow-discharged (60 s, 8 mA). Vitrification was performed on the Vitrobot Mark IV (Thermo Fisher Scientific), and the following parameters were used: 100% humidity, 277 K, 2 s blot time, 0 s wait time, blot force −1, 0 s drain time and a total blot of 1. After plunge-freezing in liquid ethane, the grids were stored in liquid nitrogen until use.

Data acquisition and processing

Cryo-EM data for all samples were collected at the National Cryo-EM Centre SOLARIS in Kraków, Poland. Datasets contained 7,784, 4,613 and 3,027 videos (40 frames each) for samples of cytb_6f with DPQ, during catalysis and with DBMIB added. Datasets were collected on a Titan Krios G3i microscope (Thermo Fisher Scientific) at an accelerating voltage of 300 kV, a magnification of ×105,000 and a pixel size of 0.86 Å per pixel (Extended Data Fig. 1a) using EPU 2.10.0.1941REL software. A K3 direct electron detector was used for data collection in a BioQuantum Imaging Filter (Gatan) set-up with a 20 eV slit width. The detector was operated in counting mode. Imaged areas were exposed to 40.7 e^- Å^{-2} (sample with DPQ and frozen during catalysis) or 41.34 e^- Å^{-2} (sample with DBMIB) total dose (corresponding to a dose rate of ~16.62 e^- per pixel per second and 15.94 e^- per pixel per second measured in vacuum, respectively). The defocus range applied was −2.1 µm to −0.9 µm with 0.3 µm steps. All datasets were processed (Extended Data Fig. 1b) using cryoSPARC v4.4.0[49–53]. Micrographs were motion-corrected using Patch Motion Correction, and the contrast transfer function (CTF) was determined using Patch CTF. In preprocessing, particles from a small portion of micrographs (50–1,000 exposures, depending on dataset quality) were extracted using the Blob picker. The obtained sets of particles were two-dimensionally classified and used for the generation of templates and particle classes for the Template picker and TOPAZ[54], respectively. Different approaches for further processing were used depending on the particular dataset quality. In the case of cytb_6f with DPQ (Extended Data Fig. 1b, left), the particles obtained from Template picker and TOPAZ were 2D classified and then sorted in ab initio reconstruction. The obtained two pools of particles (1,214,119 and 1,179,618 particles) were merged, and then duplicated particles were removed. The resulting set was cleaned using heterogeneous refinement. Particles from the final set (1,320,164) were extracted into a box of 512 pixels and used for final ab initio reconstruction followed by a non-uniform refinement. The obtained 2.04 Å map was used as an input for reference-based motion correction. The motion-corrected particles (1,320,078) were used for non-uniform refinement with iterative CTF refinement to reconstruct a final structure with 1.94 Å resolution (Extended Data Fig. 1c–f, left). For the catalytic sample of cytb_6f with DPQ, PC and DPQH$_2$ (Extended Data Fig. 1b, middle), particles extracted with Template picker were two-dimensionally classified twice and then sorted in ab initio reconstruction and heterogeneous refinement. In the case of particles extracted with TOPAZ, two-dimensional classification was omitted, and they were sorted into five classes in ab initio reconstruction and heterogenous refinement. The best particle sets from the Template picker and TOPAZ picking (251,242 and 490,927 particles, respectively) were pooled together and further sorted in ab initio reconstruction followed by heterogeneous refinement. After the removal of duplicated particles, two extractions were performed. Particles extracted into a box of 512 pixels were used for final ab initio reconstruction followed by non-uniform refinement with iterative CTF refinement. Then, the obtained 2.40 Å map was used as input for reference-based motion correction. The motion-corrected particles (482,950) were used for non-uniform refinement with iterative CTF refinement to reconstruct a final structure with 2.24 Å resolution (Extended Data Fig. 1c–f, middle). The particles extracted into a box of 384 pixels were used for 3D classification. For this purpose, after ab initio reconstruction followed by non-uniform refinement (without iterative CTF refinement, 3.02 Å map resolution), the dataset was symmetry expanded. The particles were then subjected to focused 3D classification with a generous mask encompassing the lumen side of cytochrome *f*, ISP and bound PC. The 3D classification was initially performed with 2, 4 and 6 classes. However, we found that the effective number of 3D classes is 4. After the removal of duplicate particles, maps were generated by reconstruction only to preserve the prior alignment of particles. In the case of the dataset for cytb_6f with DBMIB (Extended Data Fig. 1b, right), particles were first extracted by Template picker, 2D classified and sorted in ab initio reconstruction and heterogenous refinement. The 201,233 particles representing the best class were pooled together with particles picked by two separate TOPAZ models. Then, the particles were subjected to ab initio reconstruction and heterogenous refinement, yielding two good classes of particles, which were then processed further. After the removal of duplicates, the final extraction into a box of 384 pixels was performed, and particles were subjected to two rounds of sorting in ab initio reconstruction and heterogenous refinement. The final set of 391,430 particles was used as input in non-uniform refinement with iterative CTF refinement to reconstruct a 2.38 Å map. Then, the particles were local motion-corrected and used in a final non-uniform refinement with iterative CTF refinement to obtain a final map with 2.33 Å resolution (Extended Data Fig. 1c–f, right). Atomic models were built based on 7ZYV structure from Protein Data Bank (PDB) using ChimeraX[55] and Coot[56], refined using PHENIX[57] and validated with MolProbity[58].

EPR spectroscopy

The EPR spectra for all cytb_6f samples were measured at 10 K using a Bruker Elexsys E580 spectrometer operating at X band, equipped with a SuperHQ resonator and an ESR900 cryostat (Oxford Instruments). The temperature was set using a Lakeshore 336 temperature controller unit (Lake Shore Cryotronics). The cryogenic temperature was achieved using a Stinger cryocooler (Cold Edge Technologies). The parameters of the measurements were set as follows: microwave frequency, 9.39 GHz; microwave power, 6.35 mW; modulation amplitude, 15 G; modulation frequency, 100 kHz; sweep time, 671 s; sweep width, 4,500 G. Samples of 50 µM cytb_6f with and without DPQ added (10× excess) as well as with NQNO added (5× excess) were poised at different ambient redox potential values by adding small aliquots of sodium dithionite solution to an anaerobic, argon-flushed solution. Several redox mediators were used to stabilize the ambient redox potential as described in ref. 59.

QM calculations

The cluster model used in the quantum mechanical calculations was constructed based on the cryo-EM structure of the Q$_n$ site not occupied by quinone. The model contains haem c_n coordinated by a water molecule, 14 protein residues (D20^{b6}, K24^{b6}, Y25^{b6} (only backbone fragment), V26^{b6}, I206^{b6}, R207^{b6}, G210^{b6}, I211^{b6}, N25^{sIV}, A31^{sIV}, D35^{sIV}, L36^{sIV}, F40^{sIV} and R26^{PetN}) and 7 or 8 water molecules occupying the Q$_n$ site, which were added to fit the density. The geometry optimization was performed using the DFT/B3LYP-D3 method[60,61] combined with the def2-SVP basis set[62] to determine the position and number of water molecules occupying the active site Q$_n$. The quantum mechanical calculations were performed in Gaussian 16 (ref. 63). During optimization, haem c_n with a water ligand and all 14 protein residues were constrained according to the cryo-EM structure, and only the water molecules occupying the Q$_n$ site were optimized. Initially, based on the cryo-EM density, seven water molecules were inserted into the Q$_n$ site. However, geometry optimization indicated that to maintain the continuity of the water cluster structure, another molecule should be added to the model. Finally, the structure with eight water molecules occupying the Q$_n$ site was optimized. The results showed that for oxidized and reduced haem c_n (containing high-spin iron) cofactors, the water molecules took similar positions.

Reporting summary

Further information on research design is available in the Nature Portfolio Reporting Summary linked to this article.

Data availability

The micrographs and cryo-EM densities have been deposited in the Electron Microscopy Public Image Archive (EMPIAR) and the Electron Microscopy Data Bank (EMDB) with the following accession codes: EMPIAR-12144, EMPIAR-12158 and EMPIAR-12149, and EMD-19938, EMD-19939 and EMD-19940, respectively. The protein models have been deposited in the PDB and are accessible using the following PDB IDs: 9ES7, 9ES8 and 9ES9. All other data generated in this study are available from corresponding authors on reasonable request.

References

1. Cramer, W. A. & Kallas, T. (eds) *Cytochrome Complexes: Evolution, Structures, Energy Transduction, and Signaling* Vol. 41 (Springer, 2016).
2. Allen, J. F. Photosynthesis of ATP-electrons, proton pumps, rotors, and poise. *Cell* **110**, 273–276 (2002).
3. Sarewicz, M. et al. Catalytic reactions and energy conservation in the cytochrome bc_1 and b_6f complexes of energy-transducing membranes. *Chem. Rev.* **121**, 2020–2108 (2021).
4. Mitchell, P. The protonmotive Q cycle: a general formulation. *FEBS Lett.* **59**, 137–139 (1975).
5. Hasan, S. S., Yamashita, E. & Cramer, W. A. Transmembrane signaling and assembly of the cytochrome b_6f-lipidic charge transfer complex. *Biochim. Biophys. Acta* **1827**, 1295–1308 (2013).
6. Tikhonov, A. N. The cytochrome b_6f complex at the crossroad of photosynthetic electron transport pathways. *Plant Physiol. Biochem.* **81**, 163–183 (2014).
7. Dumas, L. et al. A stromal region of cytochrome b_6f subunit IV is involved in the activation of the Stt7 kinase in *Chlamydomonas*. *Proc. Natl Acad. Sci. USA* **114**, 12063–12068 (2017).
8. Nawrocki, W. J. et al. The mechanism of cyclic electron flow. *Biochim. Biophys. Acta* **1860**, 433–438 (2019).
9. Crofts, A. R., Meinhardt, S. W., Jones, K. R. & Snozzi, M. The role of the quinone pool in the cyclic electron-transfer chain of *Rhodopseudomonas sphaeroides* A modified Q-cycle mechanism. *Biochim. Biophys. Acta* **723**, 202–218 (1983).
10. Cape, J. L., Bowman, M. K. & Kramer, D. M. Understanding the cytochrome *bc* complexes by what they don't do. The Q-cycle at 30. *Trends Plant Sci.* **11**, 46–55 (2006).
11. Malone, L. A., Proctor, M. S., Hitchcock, A., Hunter, C. N. & Johnson, M. P. Cytochrome b_6f—orchestrator of photosynthetic electron transfer. *Biochim. Biophys. Acta* **1862**, 148380 (2021).
12. Berry, E. A. et al. X-ray structure of *Rhodobacter capsulatus* cytochrome bc_1: comparison with its mitochondrial and chloroplast counterparts. *Photosynth. Res.* **81**, 251–275 (2004).
13. Gao, X. et al. Structural basis for the quinone reduction in the bc_1 complex: a comparative analysis of crystal structures of mitochondrial cytochrome bc_1 with bound substrate and inhibitors at the Q_i site. *Biochemistry* **42**, 9067–9080 (2003).
14. Iwata, S. et al. Complete structure of the 11-subunit bovine mitochondrial cytochrome bc_1 complex. *Science* **281**, 64–71 (1998).
15. Stroebel, D., Choquet, Y., Popot, J.-L. & Picot, D. An atypical haem in the cytochrome b_6f complex. *Nature* **426**, 413–418 (2003).
16. Kurisu, G., Zhang, H., Smith, J. L. & Cramer, W. A. Structure of the cytochrome b_6f complex of oxygenic photosynthesis: tuning the cavity. *Science* **302**, 1009–1014 (2003).
17. Hasan, S. S., Yamashita, E., Baniulis, D. & Cramer, W. A. Quinone-dependent proton transfer pathways in the photosynthetic cytochrome b_6f complex. *Proc. Natl Acad. Sci. USA* **110**, 4297–4302 (2013).
18. Hasan, S. S., Proctor, E. A., Yamashita, E., Dokholyan, N. V. & Cramer, W. A. Traffic within the cytochrome b_6f lipoprotein complex: gating of the quinone portal. *Biophys. J.* **107**, 1620–1628 (2014).
19. Hasan, S. S. & Cramer, W. A. Internal lipid architecture of the hetero-oligomeric cytochrome b_6f complex. *Structure* **22**, 1008–1015 (2014).
20. Baniulis, D. et al. Structure-function, stability, and chemical modification of the cyanobacterial cytochrome b_6f complex from *Nostoc* sp. PCC 7120. *J. Biol. Chem.* **284**, 9861–9869 (2009).
21. Sarewicz, M. et al. High-resolution cryo-EM structures of plant cytochrome b_6f at work. *Sci. Adv.* **9**, eadd9688 (2023).
22. Malone, L. A. et al. Cryo-EM structure of the spinach cytochrome b_6f complex at 3.6 Å resolution. *Nature* **575**, 535–539 (2019).
23. Yamashita, E., Zhang, H. & Cramer, W. A. Structure of the cytochrome b_6f complex: quinone analogue inhibitors as ligands of heme cn. *J. Mol. Biol.* **370**, 39–52 (2007).
24. Proctor, M. S. et al. Cryo-EM structures of the *Synechocystis* sp. PCC 6803 cytochrome b_6f complex with and without the regulatory PetP subunit. *Biochem. J.* **479**, 1487–1503 (2022).
25. Roberts, A. G., Bowman, M. K. & Kramer, D. M. The inhibitor DBMIB provides insight into the functional architecture of the Q_o site in the cytochrome b_6f complex. *Biochemistry* **43**, 7707–7716 (2004).
26. Darrouzet, E., Valkova-Valchanova, M., Moser, C. C., Dutton, P. L. & Daldal, F. Uncovering the [2Fe2S] domain movement in cytochrome bc_1 and its implications for energy conversion. *Proc. Natl Acad. Sci. USA* **97**, 4567–4572 (2000).
27. Tian, H., White, S., Yu, L. & Yu, C.-A. Evidence for the head domain movement of the Rieske iron–sulfur protein in electron transfer reaction of the cytochrome bc_1 complex. *J. Biol. Chem.* **274**, 7146–7152 (1999).
28. Sarewicz, M., Dutka, M., Froncisz, W. & Osyczka, A. Magnetic interactions sense changes in distance between heme b_L and the iron–sulfur cluster in cytochrome bc_1. *Biochemistry* **48**, 5708–5720 (2009).
29. Cooley, J. W., Roberts, A. G., Bowman, M. K., Kramer, D. M. & Daldal, F. The raised midpoint potential of the [2Fe2S] cluster of cytochrome bc_1 is mediated by both the Q_o site occupants and the head domain position of the Fe–S protein subunit. *Biochemistry* **43**, 2217–2227 (2004).
30. Zhang, Z. et al. Electron transfer by domain movement in cytochrome bc_1. *Nature* **392**, 677–684 (1998).
31. Bowman, M. K., Berry, E. A., Roberts, A. G. & Kramer, D. M. Orientation of the g-tensor axes of the Rieske subunit in the cytochrome bc_1 complex. *Biochemistry* **43**, 430–436 (2004).
32. Roberts, A. G., Bowman, M. K. & Kramer, D. M. Certain metal ions are inhibitors of cytochrome b_6f complex 'Rieske' iron–sulfur protein domain movements. *Biochemistry* **41**, 4070–4079 (2002).
33. Rao, B. K. S., Tyryshkin, A. M., Roberts, A. G., Bowman, M. K. & Kramer, D. M. Inhibitory copper binding site on the spinach cytochrome b_6f complex: implications for Q_o site catalysis. *Biochemistry* **39**, 3285–3296 (2000).
34. de Lacroix de Lavalette-Boehm, A., Barucq, L., Alric, J., Rappaport, F. & Zito, F. Is the redox state of the ci heme of the cytochrome b_6f complex dependent on the occupation and structure of the Q_i site and vice versa? *J. Biol. Chem.* **284**, 20822–20829 (2009).
35. Zatsman, A. I., Zhang, H., Gunderson, W. A., Cramer, W. A. & Hendrich, M. P. Heme–heme interactions in the cytochrome b_6f complex: EPR spectroscopy and correlation with structure. *J. Am. Chem. Soc.* **128**, 14246–14247 (2006).
36. Baymann, F., Giusti, F., Picot, D. & Nitschke, W. The c_i/b_H moiety in the b_6f complex studied by EPR: a pair of strongly interacting hemes. *Proc. Natl Acad. Sci. USA* **104**, 519–524 (2007).
37. Szwalec, M., Bujnowicz, Ł., Sarewicz, M. & Osyczka, A. Unexpected heme redox potential values implicate an uphill step in cytochrome b_6f. *J. Phys. Chem. B* **126**, 9771–9780 (2022).
38. Alric, J., Pierre, Y., Picot, D., Lavergne, J. & Rappaport, F. Spectral and redox characterization of the heme c_i of the cytochrome b_6f complex. *Proc. Natl Acad. Sci. USA* **102**, 15860–15865 (2005).

39. Lavergne, J. Membrane potential-dependent reduction of cytochrome *b*-6 in an algal mutant lacking photosystem I centers. *Biochim. Biophys. Acta* **725**, 25–33 (1983).
40. Riché, A. et al. The stromal side of cytochrome b_6f complex regulates state transitions. *The Plant Cell* koae190 (2024); https://doi.org/10.1093/plcell/koae190
41. Schoepp, B., Brugna, M., Riedel, A., Nitschke, W. & Kramer, D. M. The Q_o-site inhibitor DBMIB favours the proximal position of the chloroplast Rieske protein and induces a p*K*-shift of the redox-linked proton. *FEBS Lett.* **450**, 245–250 (1999).
42. Vener, A. V., van Kan, P. J. M., Gal, A., Andersson, B. & Ohad, I. Activation/deactivation cycle of redox-controlled thylakoid protein phosphorylation: role of PLASTOQUINOL bound to the reduced cytochrome *bf* complex. *J. Biol. Chem.* **270**, 25225–25232 (1995).
43. Yan, J., Kurisu, G. & Cramer, W. A. Intraprotein transfer of the quinone analogue inhibitor 2,5-dibromo-3-methyl-6-isopropyl-p-benzoquinone in the cytochrome b_6f complex. *Proc. Natl Acad. Sci. USA* **103**, 69–74 (2006).
44. Sarewicz, M. et al. Metastable radical state, nonreactive with oxygen, is inherent to catalysis by respiratory and photosynthetic cytochromes bc_1/b_6f. *Proc. Natl Acad. Sci. USA* **114**, 1323–1328 (2017).
45. Rinalducci, S., Larsen, M. R., Mohammed, S. & Zolla, L. Novel protein phosphorylation site identification in spinach stroma membranes by titanium dioxide microcolumns and tandem mass spectrometry. *J. Proteome Res.* **5**, 973–982 (2006).
46. Zito, F. et al. The Q_o site of cytochrome b_6f complexes controls the activation of the LHCII kinase. *EMBO J.* **18**, 2961–2969 (1999).
47. Cooley, J. W. Protein conformational changes involved in the cytochrome bc_1 complex catalytic cycle. *Biochim. Biophys. Acta* **1827**, 1340–1345 (2013).
48. Porra, R. J., Thompson, W. A. & Kriedemann, P. E. Determination of accurate extinction coefficients and simultaneous equations for assaying chlorophylls *a* and *b* extracted with four different solvents: verification of the concentration of chlorophyll standards by atomic absorption spectroscopy. *Biochim. Biophys. Acta* **975**, 384–394 (1989).
49. Punjani, A., Rubinstein, J. L., Fleet, D. J. & Brubaker, M. A. cryoSPARC: algorithms for rapid unsupervised cryo-EM structure determination. *Nat. Methods* **14**, 290–296 (2017).
50. Punjani, A., Zhang, H. & Fleet, D. J. Non-uniform refinement: adaptive regularization improves single-particle cryo-EM reconstruction. *Nat. Methods* **17**, 1214–1221 (2020).
51. Rubinstein, J. L. & Brubaker, M. A. Alignment of cryo-EM movies of individual particles by optimization of image translations. *J. Struct. Biol.* **192**, 188–195 (2015).
52. Stagg, S. M., Noble, A. J., Spilman, M. & Chapman, M. S. ResLog plots as an empirical metric of the quality of cryo-EM reconstructions. *J. Struct. Biol.* **185**, 418–426 (2014).
53. Zivanov, J., Nakane, T. & Scheres, S. H. W. Estimation of high-order aberrations and anisotropic magnification from cryo-EM data sets in RELION-3.1. *IUCrJ* **7**, 253–267 (2020).
54. Bepler, T., Kelley, K., Noble, A. J. & Berger, B. Topaz-Denoise: general deep denoising models for cryoEM and cryoET. *Nat. Commun.* **11**, 5208 (2020).
55. Meng, E. C. et al. UCSF ChimeraX: tools for structure building and analysis. *Protein Sci.* **32**, e4792 (2023).
56. Emsley, P., Lohkamp, B., Scott, W. G. & Cowtan, K. Features and development of Coot. *Acta Crystallogr. D* **66**, 486–501 (2010).
57. Adams, P. D. et al. PHENIX: a comprehensive Python-based system for macromolecular structure solution. *Acta Crystallogr. D* **66**, 213–221 (2010).
58. Davis, I. W. et al. MolProbity: all-atom contacts and structure validation for proteins and nucleic acids. *Nucleic Acids Res.* **35**, W375–W383 (2007).
59. Sarewicz, M., Pintscher, S., Bujnowicz, Ł., Wolska, M. & Osyczka, A.The high-spin heme b_L mutant exposes dominant reaction leading to the formation of the semiquinone spin-coupled to the [2Fe-2S]+ cluster at the Q_o site of *Rhodobacter capsulatus* cytochrome bc_1. *Front. Chem.* **9**, 658877 (2021).
60. Grimme, S., Antony, J., Ehrlich, S. & Krieg, H. A consistent and accurate ab initio parametrization of density functional dispersion correction (DFT-D) for the 94 elements H-Pu. *J. Chem. Phys.* **132**, 154104 (2010).
61. Grimme, S., Ehrlich, S. & Goerigk, L. Effect of the damping function in dispersion corrected density functional theory. *J. Comput. Chem.* **32**, 1456–1465 (2011).
62. Weigend, F. & Ahlrichs, R. Balanced basis sets of split valence, triple zeta valence and quadruple zeta valence quality for H to Rn: design and assessment of accuracy. *Phys. Chem. Chem. Phys.* **7**, 3297–3305 (2005).
63. Frisch, M. J. et al. *Gaussian 16, Revision C.01* (Gaussian, 2016).

Acknowledgements

We thank all members of the Osyczka and Glatt laboratories for discussion and suggestions. This work was supported by the Team grant (POIR.04.04.00-00-5B54/17-00 to A.O.) and the Team Tech core facility grant (TEAM TECH CORE FACILITY/2017-4/6 to S.G.) from the Foundation for Polish Science, and the OPUS-24 grant (2022/47/B/NZ1/03308 to A.O.) from NCN. The work is supported under the Polish Ministry of Education and Science project: 'Support for research and development with the use of research infrastructure of the National Synchrotron Radiation Centre SOLARIS' under contract number 1/SOL/2021/2. We also acknowledge the Polish high-performance computing infrastructure PLGrid (HPC Center: ACK Cyfronet AGH) for providing computer facilities and support within computational grant numbers PLG/2022/015736, PLG/2022/015891 and PLG/2023/016614. The open access of this article was funded by the Priority Research Area BioS under the program 'Initiative of Excellence - Research University' at the Jagiellonian University in Kraków. We also acknowledge infrastructural support from this programme.

Author contributions

The study was designed and directed by S.G. and A.O. R.P. and B.M. isolated and purified cytb_6f complexes. S.P. isolated and purified PC. S.P., R.P. and B.M. prepared cryo-EM samples. G.W. and S.P. performed initial grid screening and grid optimization. Data collection was done by M.J., P.I., G.W. and M.R. Data processing was done by S.P., M.J. and Ł.K. Map interpretation, model building and refinement were done by S.P. and R.P. with the help of M.J., Ł.K. and S.G. M.S. performed EPR experiments. A.W.-A. performed QM calculations and analysis. Figures were prepared by S.P., R.P. and B.M. with support from S.G. and A.O. The paper was written by S.P., R.P., S.G. and A.O., with all authors discussing the results and refining and approving the final version.

Competing interests

The authors declare no competing interests.

Additional information

Extended data is available for this paper at https://doi.org/10.1038/s41477-024-01804-x.

Supplementary information The online version contains supplementary material available at https://doi.org/10.1038/s41477-024-01804-x.

Correspondence and requests for materials should be addressed to Sebastian Glatt or Artur Osyczka.

Peer review information *Nature Plants* thanks Jean Alric and Michael Hippler for their contribution to the peer review of this work.

Reprints and permissions information is available at www.nature.com/reprints.

Publisher's note Springer Nature remains neutral with regard to jurisdictional claims in published maps and institutional affiliations.

Open Access This article is licensed under a Creative Commons Attribution-NonCommercial-NoDerivatives 4.0 International License, which permits any non-commercial use, sharing, distribution and reproduction in any medium or format, as long as you give appropriate credit to the original author(s) and the source, provide a link to the Creative Commons licence, and indicate if you modified the licensed material. You do not have permission under this licence to share adapted material derived from this article or parts of it. The images or other third party material in this article are included in the article's Creative Commons licence, unless indicated otherwise in a credit line to the material. If material is not included in the article's Creative Commons licence and your intended use is not permitted by statutory regulation or exceeds the permitted use, you will need to obtain permission directly from the copyright holder. To view a copy of this licence, visit http://creativecommons.org/licenses/by-nc-nd/4.0/.

© The Author(s) 2024

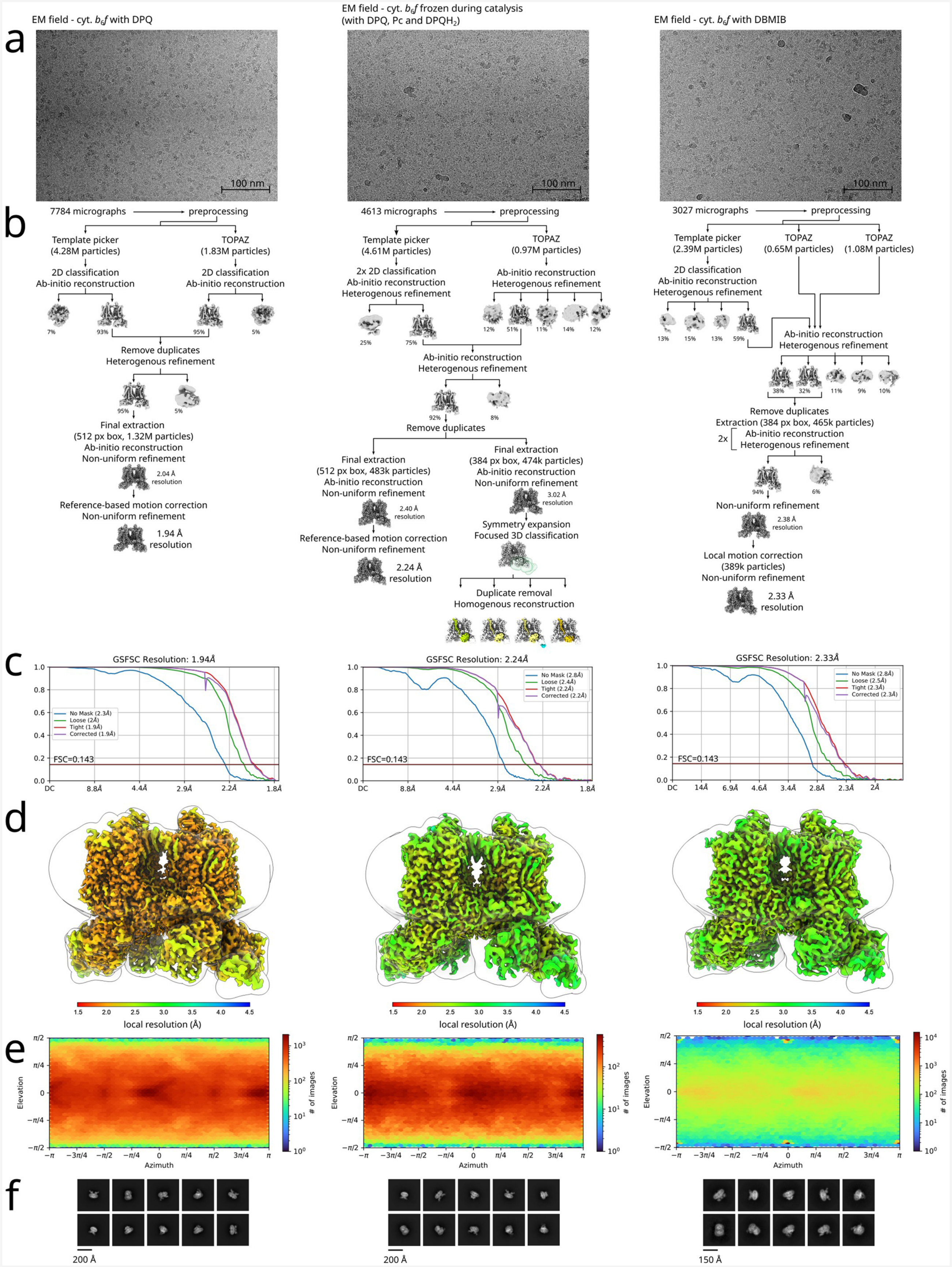

Extended Data Fig. 1 | Cryo-EM data processing workflow. Cryo-EM datasets processing for cytb_6f with DPQ (1.9 Å map; EMD-19938), cytb_6f frozen under turnover conditions (2.2 Å map; EMD-19939) and cytb_6f with DBMIB (2.3 Å map; EMD-19940); left, middle and right, respectively. **a**, representative cryo-EM fields; **b**, cryoSPARC processing pipelines; **c**, Fourier shell correlation curves, dark red lines in the plots indicate FSC = 0.143; **d**, local-filtered maps colored by resolution range; **e**, particle angular distribution heatmaps calculated in cryoSPARC; **f**, selected 2D class averages for the particles contributing to the respective maps.

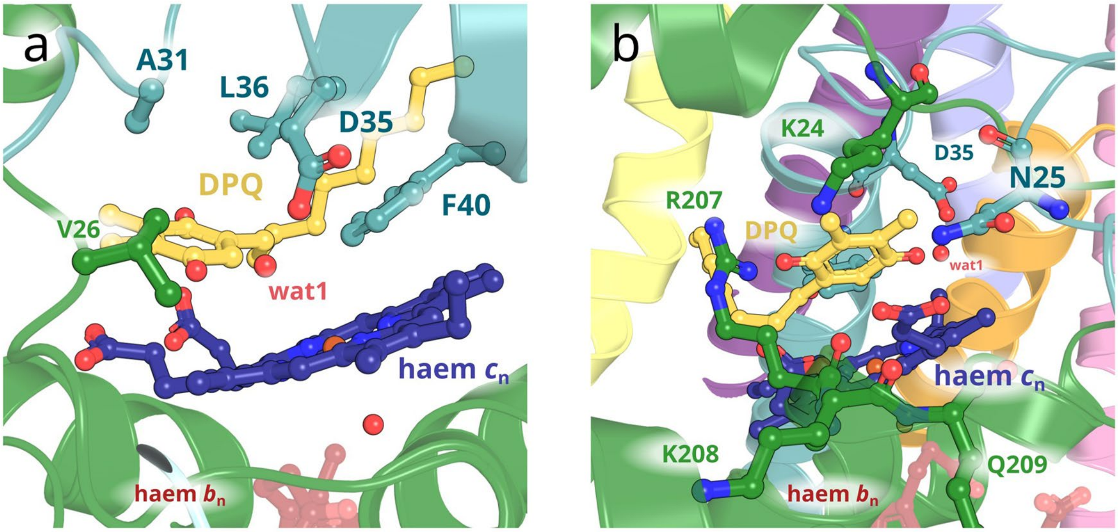

Extended Data Fig. 2 | Additional views on quinone in Q_n site of cytb_6f. Additional close-up views on quinone in Q_n of cytb_6f taken from 2.2 Å structure, PDB ID: 9ES8. **a**, ring of hydrophobic sidechains around wat1 and D35$^{\mathrm{sIV}}$; **b**, the hydrophilic environment around one of the haem c_n propionates groups ('distal propionate').

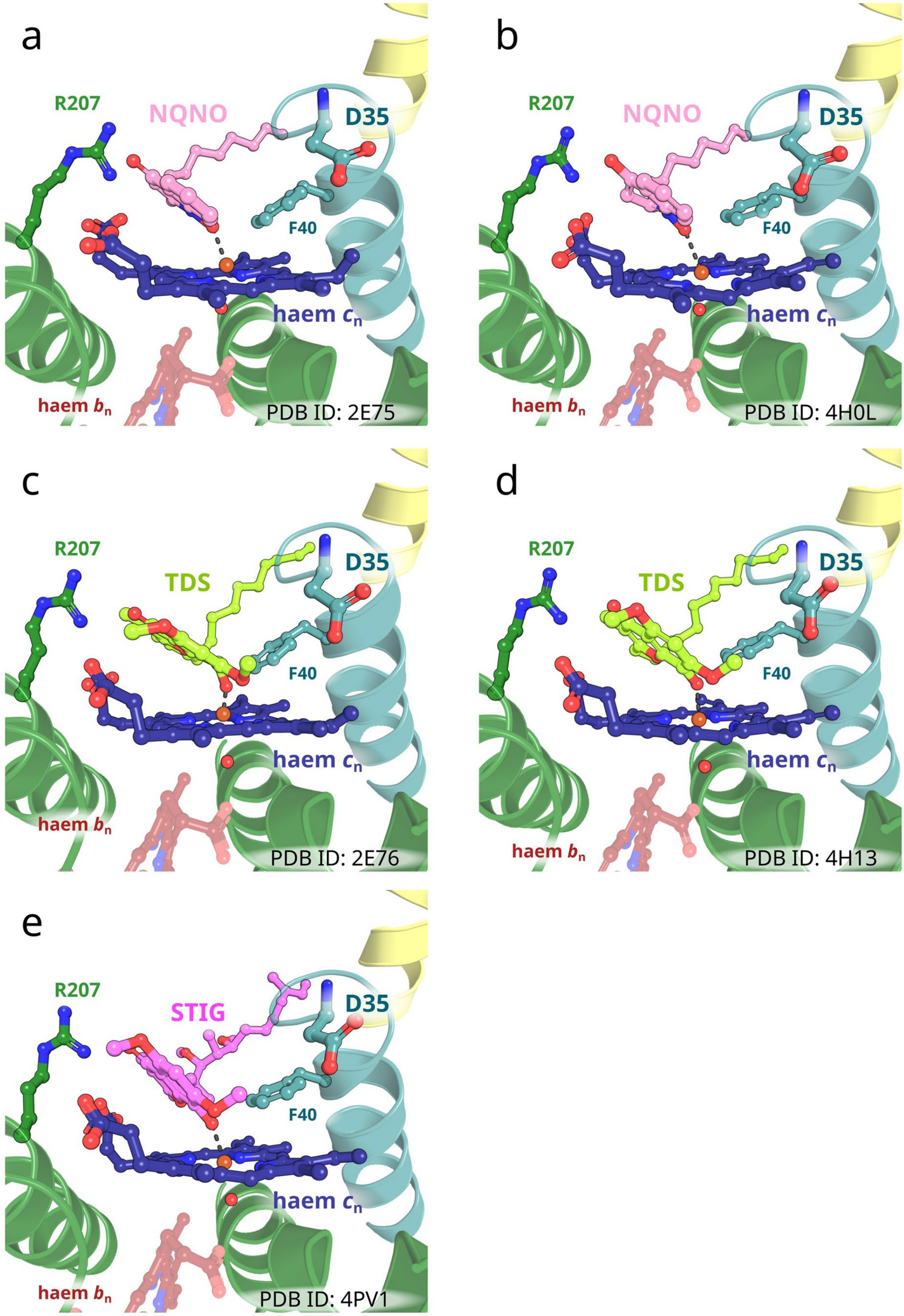

Extended Data Fig. 3 | Inhibitors in Q_n site of cyt*b*$_6$*f*. Close-up views on Q_n of *Mastigocladus laminosus* cyt*b*$_6$*f* with different inhibitors. **a**, 2-nonyl-4-hydroxyquinoline N-oxide (NQNO), PDB ID: 2E75[23]; **b**, NQNO, PDB ID: 4H0L[17]; **c**, tridecyl-stigmatellin (TDS), PDB ID: 2E76[23]; **d**, TDS, PDB ID: 4H13[17]; **e**, stigmatellin-A, PDB ID: 4PV1[18].

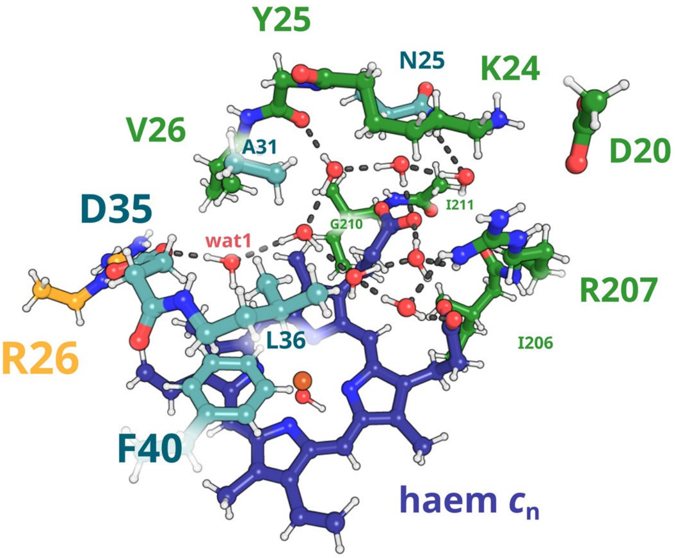

Extended Data Fig. 4 | Water molecules in Q_n site predicted from QM simulation. Geometry of QM model with optimized positions of eight water molecules at Q_n.

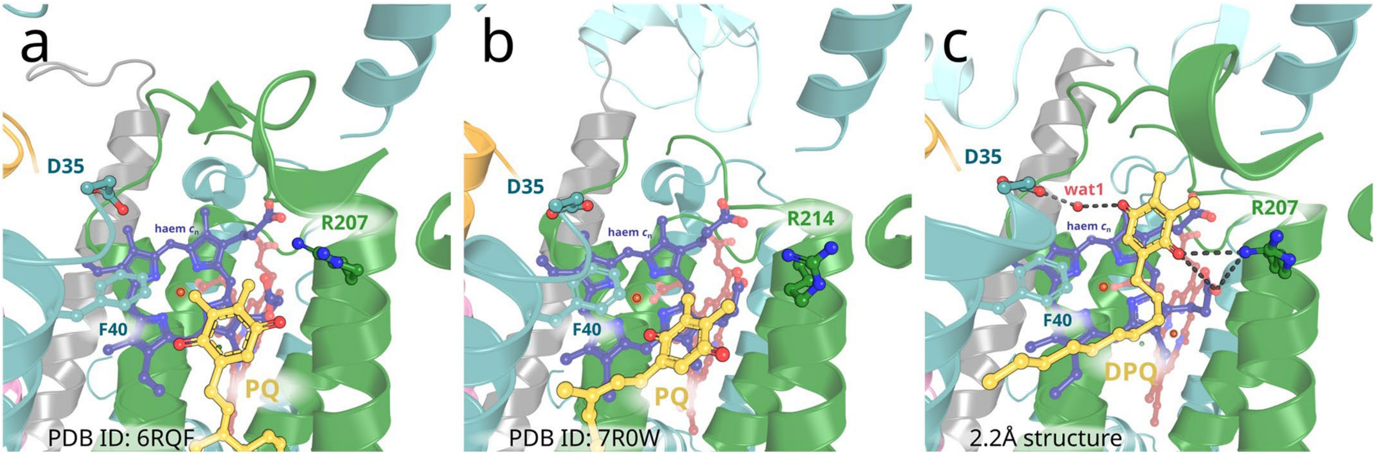

Extended Data Fig. 5 | Comparison of quinone positions in the region of Q_n site across different structures. a, PQ molecule reported for *Spinacia oleracea* (PDB ID: 6RQF). **b**, PQ molecule reported for *Synechocystis sp*. PCC 6803 (PDB ID: 7R0W). **c**, DPQ in orientation modelled in our map (PDB ID: 9ES8).

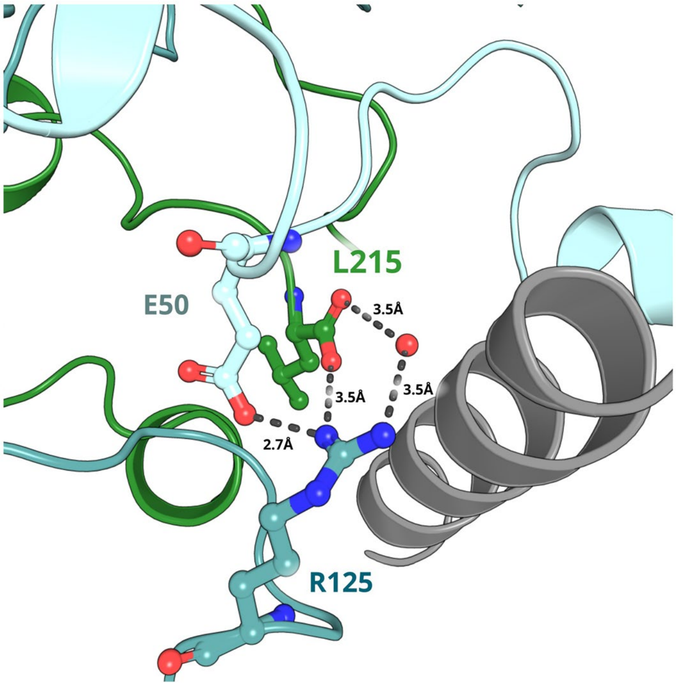

Extended Data Fig. 6 | Close-up view on the interaction between TSP9 and cyt*b*$_6$*f*. Color code: TSP9 - cyan; cyt *b* -, green; subunit IV – light teal; PetG - grey. E50$^{\mathrm{TSP9}}$ forms a salt bridge with R125$^{\mathrm{sIV}}$ which also forms a bridge with L215$^{\mathrm{b6}}$. The formation / braking of the latter bridge has been shown to have important regulatory consequences, as described in[7,40].

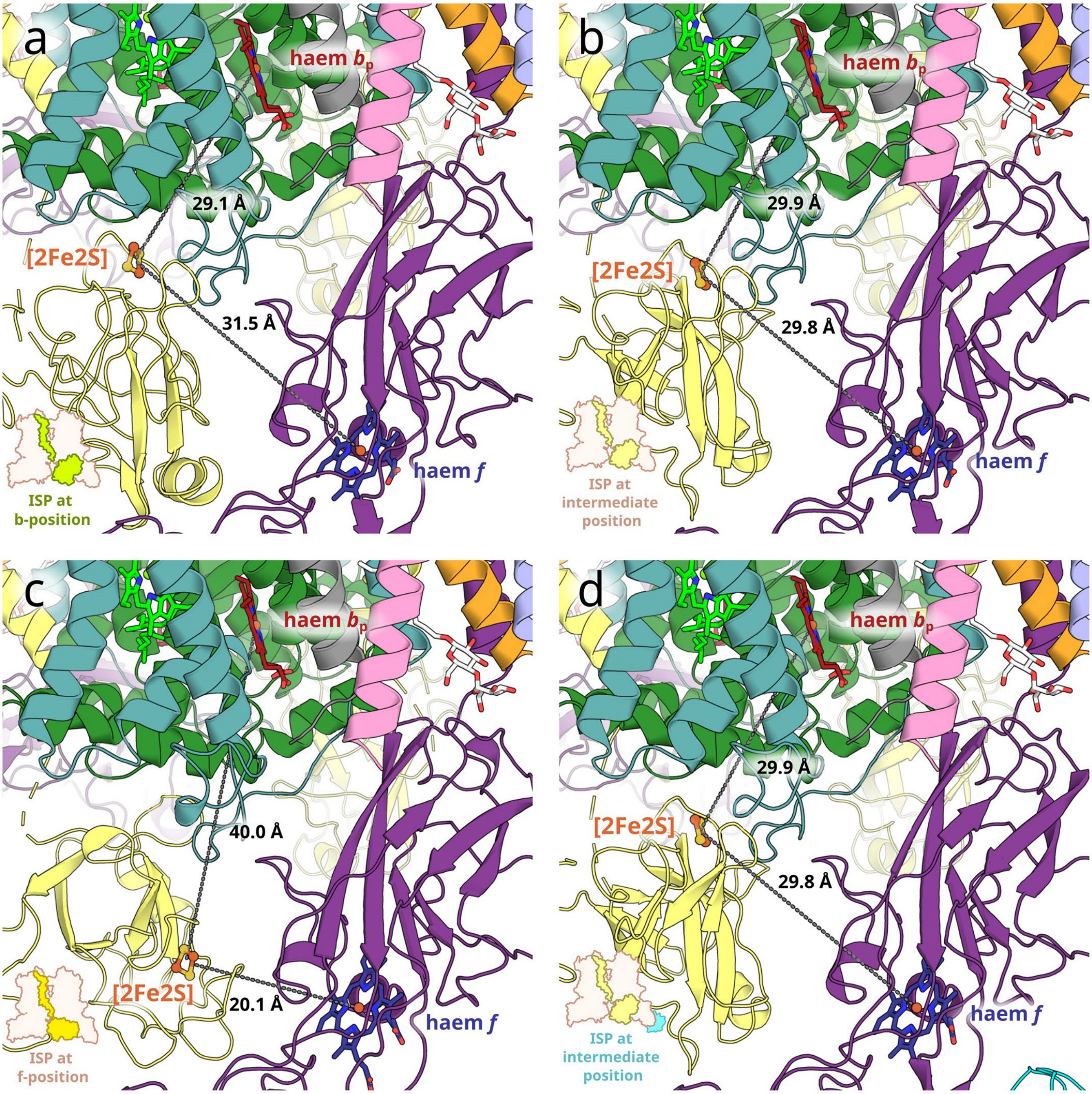

Extended Data Fig. 7 | The movement of iron-sulphur protein head domain. Distances between 2Fe2S cluster and haem *f* and haem b_p for different positions of ISP-HD. **a**, for the subgroup with ISP-HD at b-position; **b**, for the subgroup with ISP-HD at intermediate position; **c**, for the subgroup with ISP-HD at f-position; **d**, for the subgroup with ISP-HD at intermediate position with PC bound (note that position of ISP-HD is as in subgroup shown in b and the only difference is the presence of PC).

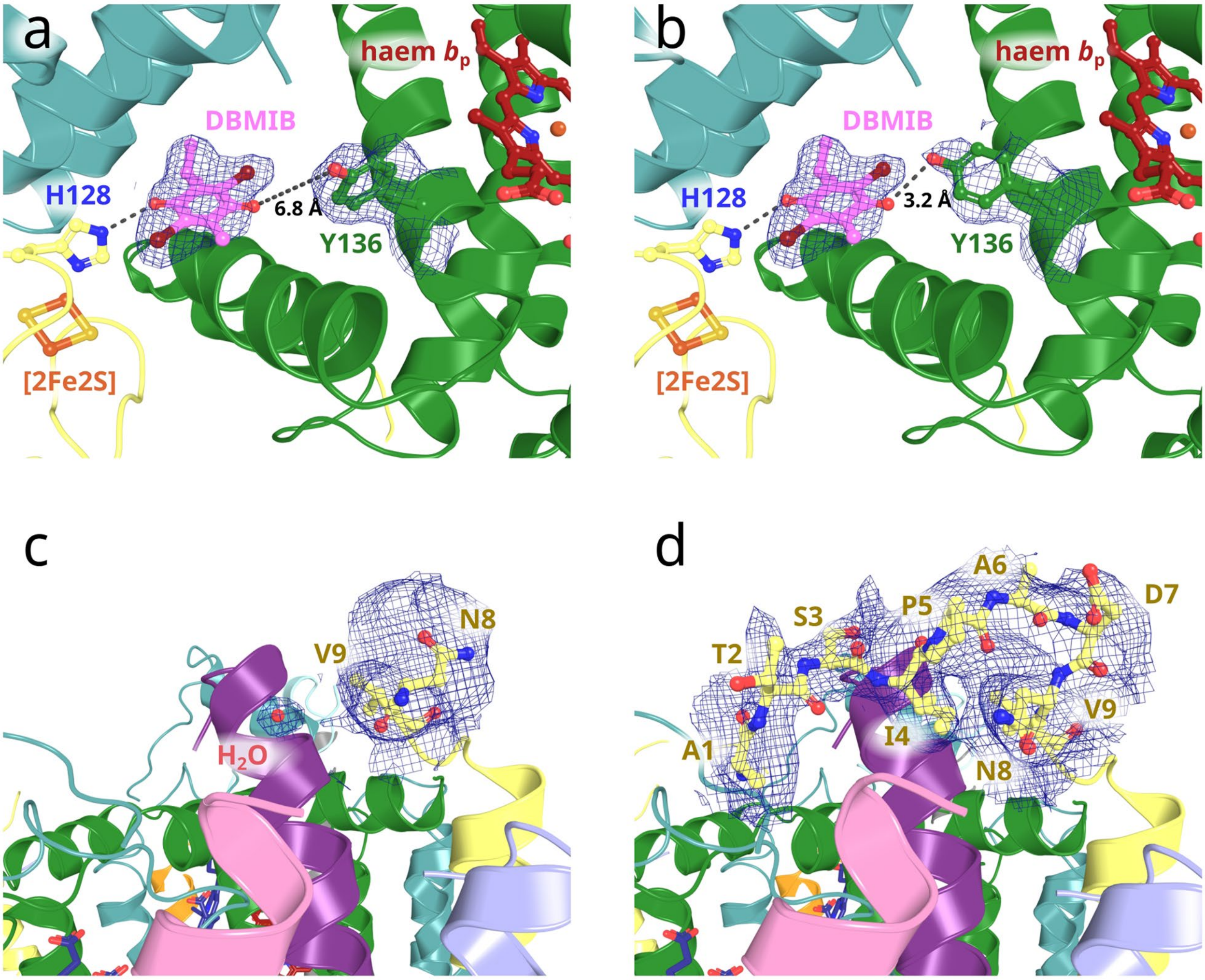

Extended Data Fig. 8 | Structural features in cytb_6f with DBMIB bound. Alternative conformations of Y136^{b6} in cytb_6f structure with DBMIB (PDB ID: 9ES9). The Y136^{b6} side-chain is placed away from or close to the DBMIB molecule (**a** and **b**, respectively). Close-up view on the membranous n-side region around the N-terminus of the ISP subunit in 1.9 Å structure (PDB ID: 9ES7) (**c**) and the structure with DBMIB (PDB ID: 9ES9) (**d**).

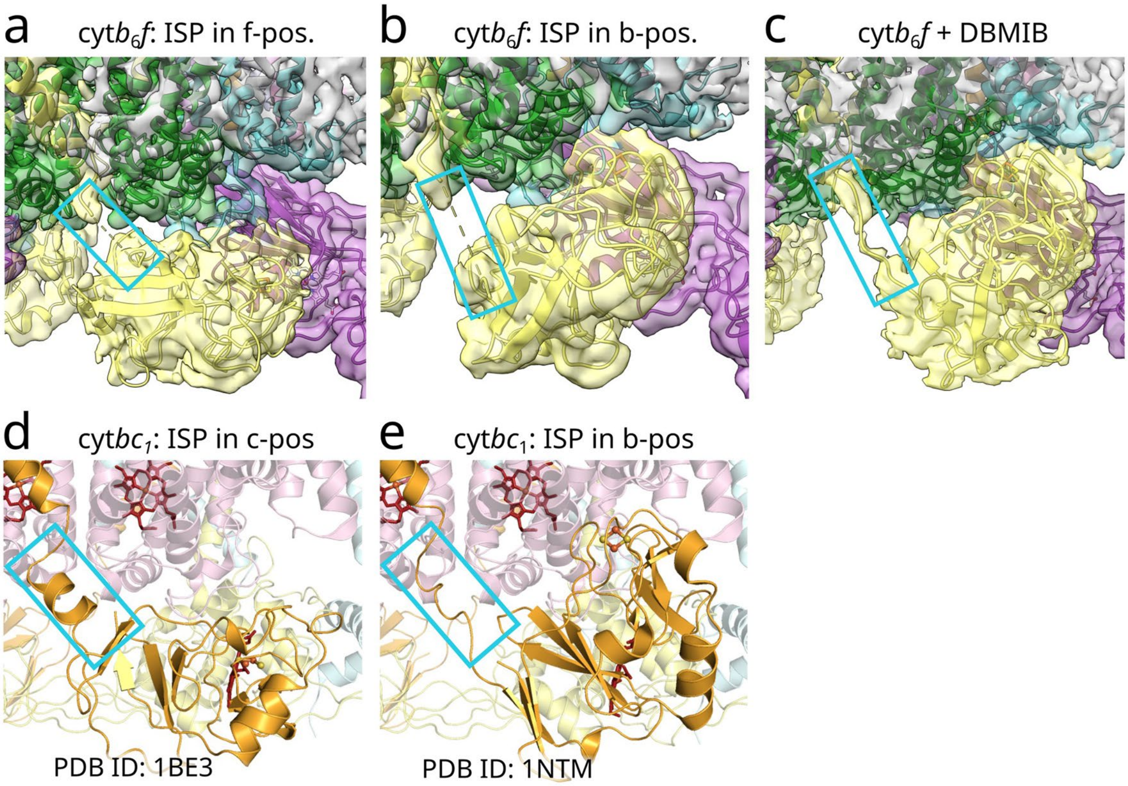

Extended Data Fig. 9 | Comparison of ISP neck region structure between cyt*b*$_6$*f* and cyt*bc*$_1$. **a**, and **b**, cryo-EM maps obtained from 3D classification of cyt*b*$_6$*f* particles frozen during catalysis (ISP head domain was in f- or b-position, respectively). The low intensity of the map of the ISP neck (sequence: GGAGTG) indicates high flexibility of the peptide backbone in this region. **c**, When DBMIB is bound to cyt*b*$_6$*f* (PDB ID: 9ES9), the ISP locks in b-position and the ISP neck becomes more rigid and this region is better resolved. The ISP neck in cyt*bc*$_1$ behaves differently: when ISP is in c-position the ISP neck forms α-helix[14] (**d**), when ISP is in the b-position, the helix is stretched[13] (**e**).

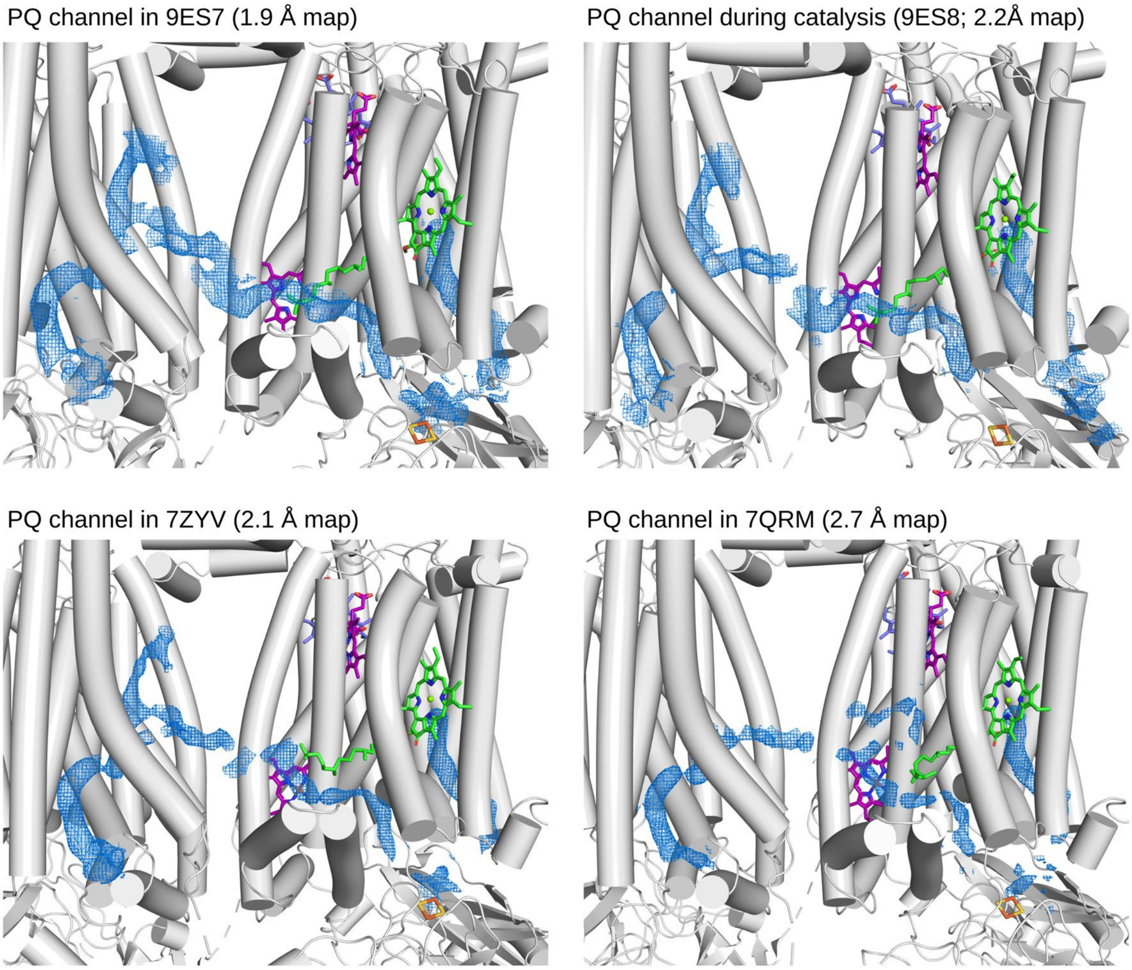

Extended Data Fig. 10 | Quinone channel in cytochrome b_6f. Cryo-EM map densities in the PQ channel area at the Q_p side in two maps reported in this paper (top) compared to our previous report (bottom).

nature portfolio

Corresponding author(s): Sebastian Glatt and Artur Osyczka

Last updated by author(s): Aug 9, 2024

Reporting Summary

Nature Portfolio wishes to improve the reproducibility of the work that we publish. This form provides structure for consistency and transparency in reporting. For further information on Nature Portfolio policies, see our Editorial Policies and the Editorial Policy Checklist.

Statistics

For all statistical analyses, confirm that the following items are present in the figure legend, table legend, main text, or Methods section.

n/a	Confirmed	
☒	☐	The exact sample size (*n*) for each experimental group/condition, given as a discrete number and unit of measurement
☒	☐	A statement on whether measurements were taken from distinct samples or whether the same sample was measured repeatedly
☒	☐	The statistical test(s) used AND whether they are one- or two-sided *Only common tests should be described solely by name; describe more complex techniques in the Methods section.*
☒	☐	A description of all covariates tested
☒	☐	A description of any assumptions or corrections, such as tests of normality and adjustment for multiple comparisons
☒	☐	A full description of the statistical parameters including central tendency (e.g. means) or other basic estimates (e.g. regression coefficient) AND variation (e.g. standard deviation) or associated estimates of uncertainty (e.g. confidence intervals)
☒	☐	For null hypothesis testing, the test statistic (e.g. *F*, *t*, *r*) with confidence intervals, effect sizes, degrees of freedom and *P* value noted *Give P values as exact values whenever suitable.*
☒	☐	For Bayesian analysis, information on the choice of priors and Markov chain Monte Carlo settings
☒	☐	For hierarchical and complex designs, identification of the appropriate level for tests and full reporting of outcomes
☒	☐	Estimates of effect sizes (e.g. Cohen's *d*, Pearson's *r*), indicating how they were calculated

Our web collection on statistics for biologists contains articles on many of the points above.

Software and code

Policy information about availability of computer code

Data collection	EPU v. 2.10.0.1941REL (Thermo Fisher)
Data analysis	cryoSPARC 4.4.0, ChimeraX 1.7, Coot 0.9.8, PHENIX 1.20.1-4487, MolProbity 4.02b-467, Topaz v0.2.4

For manuscripts utilizing custom algorithms or software that are central to the research but not yet described in published literature, software must be made available to editors and reviewers. We strongly encourage code deposition in a community repository (e.g. GitHub). See the Nature Portfolio guidelines for submitting code & software for further information.

Data

Policy information about availability of data

All manuscripts must include a data availability statement. This statement should provide the following information, where applicable:

- Accession codes, unique identifiers, or web links for publicly available datasets
- A description of any restrictions on data availability
- For clinical datasets or third party data, please ensure that the statement adheres to our policy

The micrographs and cryo-EM densities have been deposited in the Electron Microscopy Public Image Archive (EMPIAR) and the Electron Microscopy Data Bank (EMDB) with the following accession codes: EMPIAR-12144, EMPIAR-12158, EMPIAR-12149 and EMD-19938, EMD-19939, EMD-19940, respectively. The protein models have been deposited in the PDB and are accessible using the following PDB IDs: 9ES7, 9ES8, and 9ES9. All other data generated in this study are available from corresponding authors on reasonable request.

Research involving human participants, their data, or biological material

Policy information about studies with human participants or human data. See also policy information about sex, gender (identity/presentation), and sexual orientation and race, ethnicity and racism.

Reporting on sex and gender	n/a
Reporting on race, ethnicity, or other socially relevant groupings	n/a
Population characteristics	n/a
Recruitment	n/a
Ethics oversight	n/a

Note that full information on the approval of the study protocol must also be provided in the manuscript.

Field-specific reporting

Please select the one below that is the best fit for your research. If you are not sure, read the appropriate sections before making your selection.

☒ Life sciences ☐ Behavioural & social sciences ☐ Ecological, evolutionary & environmental sciences

For a reference copy of the document with all sections, see nature.com/documents/nr-reporting-summary-flat.pdf

Life sciences study design

All studies must disclose on these points even when the disclosure is negative.

Sample size	For cryo-EM analyses, details of the sample size are listed in the Extended Data Figure 1. The sample size was chosen so that high resolution structures are constructed. The number of collected micrographs mainly depends on the available time slots on the cryo-TEM - the number of particles depends on the observable and identifiable number of particles on all collected micrographs of a given dataset. The number of particles that are used for the final reconstruction typically represents only a fraction of identified particles. The required number of particles is assessed during initial screening sessions and collection of test datasets, but a reasonable compromise has to be found between available microscope time and the needed particle number to achieve a given resolution for a specific protein. In case of EPR spectroscopy, sample size corresponds to choice of appropriate protein concentration to obtain the highest possible signal-to-noise ratio of the spectra.
Data exclusions	For cryo-EM analyses, several iterations of reference-free 2D class averaging and unsupervised 3D classification were used to remove particles that do not contribute to a high-resolution 3D reconstruction.
Replication	Single particle cryo-EM is based on the averaging spatial information from a large number of individual particles within a given dataset. The 3D structure is determined and refined for a given subset of particles. Biological information is extracted from these structures and replicating the dataset could lead to the selection of slightly different subsets. Therefore, replication (in the sense of collecting independent datasets) is not an indicator for the quality of a given reconstruction. EPR spectra reflect physical properties of the studied system. Therefore, replication will neither alter the shape nor improve the quality of the obtained spectra.
Randomization	No specific randomization was used in this study. Randomization is not relevant for this study because the experiments did not require allocation of individuals into groups. Of note, individual cryo-EM particles are processed in a random fashion, which is important to avoid any bias during the structure determination.
Blinding	No specific blinding was used for the experiments presented in the study. Blinding is not relevant to cryo-EM and biophysical analyses in this study. As cryo-EM datasets are too large to be processed by hand, the risk of a subjective analyses are extremely low and blinding would not add additional value during the data processing. Of note, map interpretation and data analyses were independently carried out by various authors in parallel and discussed openly during joint meetings. In the biophysical analyses, the recorded spectra reflect the inherent physical properties of the studied system thus they cannot be biased by the operator.

Reporting for specific materials, systems and methods

We require information from authors about some types of materials, experimental systems and methods used in many studies. Here, indicate whether each material, system or method listed is relevant to your study. If you are not sure if a list item applies to your research, read the appropriate section before selecting a response.

Materials & experimental systems

n/a	Involved in the study
☒	☐ Antibodies
☒	☐ Eukaryotic cell lines
☒	☐ Palaeontology and archaeology
☒	☐ Animals and other organisms
☒	☐ Clinical data
☒	☐ Dual use research of concern
☒	☐ Plants

Methods

n/a	Involved in the study
☒	☐ ChIP-seq
☒	☐ Flow cytometry
☒	☐ MRI-based neuroimaging

Plants

Seed stocks	n/a
Novel plant genotypes	n/a
Authentication	n/a